Structure of a quantum vortex tangle in ^{4}He counterflow turbulence

Luiza Kondaurova,[1] Victor L'vov,[2] Anna Pomyalov,[2] and Itamar Procaccia[2]
[1]*Institute of Thermophysics, Novosibirsk, Russia*
[2]*Department of Chemical Physics, The Weizmann Institute of Science, Rehovot 76100, Israel*
(Received 17 July 2013; revised manuscript received 17 October 2013; published 7 January 2014)

The paper presents a comprehensive characterization of well-developed vortex tangles in a turbulent counterflow in quantum fluids (with a laminar normal fluid component). We perform and analyze extensive numerical simulations using the vortex filament method, solving the full Biot-Savart equations for the vortex dynamics in a wide range of temperatures and counterflow velocities. We start with the analysis of the macroscopic characteristics of the quantum vortex tangle such as vortex line density, its mean anisotropic and curvature parameters, the mean friction force between normal and superfluid components, the drift velocity of the vortex tangle, etc. Next we proceed to the main goal of the paper and move from the traditional macroscopic approach in terms of mean characteristics of the vortex tangle to the microscopic statistical and kinetic levels of description of quantum turbulence. These include objects that are much less studied or even totally neglected such as the vortex reconnection rates, the correlations and probability distribution functions (PDFs) of the vortex loop lengths, of the line curvature, of the mean curvatures of individual loops, the cross-correlation function between the loop length and its mean curvature, and the autocorrelation function of the vortex-line orientations. This detailed statistical information is required for a deeper understanding of quantum turbulence and for the development of its advanced theoretical description. In addition, we identify which of the studied properties are strongly affected by the choice of the reconnection criteria that are traditionally used in the vortex filament method and which of them are practically insensitive to the reconnection procedure. We conclude that the vortex filament method is sufficiently robust and well-suited for the description of the steady-state vortex tangle in the quantum counterflow.

DOI: 10.1103/PhysRevB.89.014502 PACS number(s): 67.25.dk

I. INTRODUCTION

The term "quantum turbulence" or "superfluid turbulence" refers to a tangle of interacting quantized vortex lines, which are formed, for example, in superfluid ^{4}He, ^{3}He, or in Bose-Einstein condensates of ultracold atoms. The vorticity in superfluids is restricted to a set of vortex lines around which the circulation is quantized to multiples of the circulation quantum $\kappa = h/m$. Here, h is Plank's constant and m is the mass of either atoms with integer spin, like ^{4}He, or Cooper pairs of ^{3}He atoms. In ^{4}He, $\kappa \approx 9.97 \times 10^{-4}$ cm^2/s. The creation of sustained quantum turbulence can be achieved by either mechanical excitations [1–8], or by heat currents (so-called counterflow turbulence). Experimental studies of thermal counterflow, initiated almost sixty years ago by Vinen [9,10], became the most extensively studied forms of quantum turbulence [11–16].

In the context of the popular two-fluid model of superfluids, the phenomenon of thermal counterflow may be considered as consisting of two interpenetrating fluid flows: a normal viscous component flowing in the direction of the temperature gradient and carrying the heat flux, and an inviscid superfluid component flowing in the opposite direction to keep a zero total mass transfer. These two components may have different velocity and density fields: $\boldsymbol{v}_{\rm n}(\boldsymbol{r},t)$, $\boldsymbol{v}_{\rm s}(\boldsymbol{r},t)$ and $\rho_{\rm n}(\boldsymbol{r},t)$, $\rho_{\rm s}(\boldsymbol{r},t)$. More sophisticated arrangements [17] allow one to realize (mechanically driven) pure superflows in a relatively wide (7–10 mm) channel, with the normal fluid component practically at rest. In both arrangements, a dense vortex tangle is excited under the influence of the velocity difference between the two-component quantum turbulence.

Some statistical properties of quantum vortex tangles in counter- and superflows were studied experimentally and numerically [9–24], Among the seminal contributions to these studies we should mention pioneering works by Vinen [9,10] and Schwarz [19]. In particular, in Refs. [9,10] Vinen suggested a phenomenological description of space homogeneous counterflow turbulence, Eq. (17), in terms of the vortex line density per unit volume, $\mathcal{L}$, sometimes referred as VLD. Schwarz [19] analytically established some important bridge relationships between the mean characteristics of the vortex tangle, like the mean intervortex distance $\ell \equiv 1/\sqrt{\mathcal{L}}$, the mean curvature of the vortex lines, etc. He also pioneered numerical simulations of the counterflow turbulence, proposing to use a vortex filament method (sometimes referred to as VFM) in which minor core variations of the quantized vortices are ignored and the vortices are approximated as directional lines with a predefined core structure. If so, the time evolution of these vortex lines is governed by the Biot-Savart equation (10a), according to which each point of the vortex line is swept by the velocity field produced by the entire tangle. Schwarz [19] used the so-called local induction approximation to Eq. (10a) (see Sec. IIIA2), which accounts only for "local" contribution to the vortex velocity at some point $\boldsymbol{r}$, proportional to vortex-line curvature at this point. Later Adachi, Fujiyama, and Tsubota [22] demonstrated that for an adequate numerical study of the counterflow turbulence one has to relax this approximation and to use the full Biot-Savart equation (10a) for the description of the vortex tangle evolution.

Notice that in the typical counterflow experiments, the vortex tangle is dense in the sense that the intervortex distance ℓ is much smaller than the characteristic size of the experimental cell H, which is about 1 cm. At the same time, the tangle is sparse enough such that ℓ is much larger than the vortex core radius $a_0 \approx 1.3 \times 10^{-8}$ cm in ^{4}He. Therefore, in these experiments, there is a large intermediate region of scales

$a_0 \ll \ell \ll H$ in which the evolution of the vortex tangle can be followed by the vortex filament method, as suggested by Schwarz [18,19].

During temporal evolution, the vortex lines can collide and reconnect changing the tangle's topology. Thus vortex loops can merge or break up into smaller loops. These reconnections occur on scales comparable with the vortex core radius and ignored by the Biot-Savart equation. They are included in vortex filament methods as an additional artificial procedure that changes the connectivity of pairs of points according to some reconnection criterion. The reconnection criteria are based on a physical intuition and the results of numerical simulations.

The complementary information on the vortex tangle dynamics, which is difficult or even impossible to get from the vortex-filament method, may be obtained in the framework of the Gross-Pitaevskii equations equation [29,30]. It describes, in particular, the vortex reconnections [31–34], the effect of finite amplitude Kelvin waves on the counterflow dynamics [35], the interaction of noncondensed particles with vortex rings [36], etc. By construction, the Gross-Pitaevskii simulations have to resolve the structure of the vortex core, therefore they are usually oriented towards small scale dynamics, while the vortex-filament method, on the other hand, does not have to resolve the vortex core scale and thus may be focused on studies of large vortex tangles.

Nowadays, powerful computers allow partial overlap of the scales and total line lengths available to these two methods. For example, energy spectra of large-scale quantum turbulence were successfully studied within the Gross-Pitaevskii framework [37–41] and by the vortex-filament method [42–44].

Notice that in the counterflow turbulence the main attention was given to studies of the vortex line density and its dependence on the counterflow velocity and the temperature. The other mean characteristics of the vortex tangle, such as mean tangle anisotropy and the vortex line curvature, the mean friction force between normal and superfluid components, and the drift velocity of the vortex tangle, were much less studied, see, e.g., recent reviews [25–28]. Therefore our first goal was to fill this gap, presenting in Sec. V results of comprehensive studies of the above mentioned values in counterflow turbulence for a wide range of parameters: at low, medium, and high temperatures T (1.3, 1.6, and 1.9 K) and the counterflow velocities V_{ns} ranging from 0.3 to 1.2 cm/s.

This level of description is similar to the thermodynamical approach to gases and fluids that deals with the mean (macroscopic) characteristics of the continuous media such as temperature, pressure, density, etc., averaged over finite (physical) volume. A more advanced, microscopic description of continuous media was reached in statistical physics and kinetics in the framework of probability distribution functions, PDFs, (e.g., Maxwell-Boltzmann PDF of atomic velocities) and correlation functions (e.g., of atomic positions). Similarly, the measurable mean characteristics of the vortex tangle provide important but very limited information on the tangle properties.

Therefore the main goal of this paper is to move from macroscopic to microscopic level of description of counterflow quantum turbulence in terms of PDFs and correlation functions. This statistical information is needed for deeper and more detailed understanding of quantum turbulence and for development of its advanced theoretical models, see, e.g., a recent review by Nemirovski [27]. Unfortunately, there is not much chance that detailed statistical information on quantum vortex tangle can be subject to experimental study. Therefore the numerical characterization of detailed local vortex tangle statistics is important and timely. Our corresponding results are presented in the central Sec. VI of our paper. Because of computer limitations, comprehensive statistical information on large vortex tangles with global size essentially exceeding the intervortex distance currently cannot be obtained by the Gross-Pitaevsky simulations. Therefore we used for our studies the vortex filament approach, solving full Biot-Savart equations for the vortex dynamics.

On this way we faced an old problem of the possible dependence of the numerical results within the vortex-filament simulations on the choice reconnection criteria. The reconnections of the vortex lines were recently visualized experimentally [45]. Since the method introduction by Schwarz [18,19], a number of different criteria [20,22,29,46–49] were introduced and modified over time. Currently, three criteria are frequently used to trigger the reconnections during the evolution of the vortex tangle. These are based either on geometrical proximity [22,29,48] or on the dynamics of vortex filaments [49–51], leading to a different number of reconnections and various changes in the vortex tangle topology. The presence of variety of artificial reconnection procedures in vortex filament methods and the spread in values of basic characteristics of the tangle, such as the vortex reconnection rates and steady-state vortex line density $\mathcal{L}$, resulted in the superfluid community sharing an opinion that was made explicit recently by Skrbek and Sreenivassan: [25] "while it is clear that the full Biot-Savart approach is certainly better [than the local induction approximation (LIA), see below], there are still other aspects such as approach to vortex reconnections and influence of possible normal fluid turbulence that make the predictive power of these simulations limited at the best."

Therefore, to justify our numerical results, we had to answer the question: to what extent can one state that the statistical properties of the developed vortex tangles obtained by vortex filament methods (in a wide range of parameters) are robust under changes of the reconnection procedures and other implementation details? To do this, we compared throughout the entire study, results of vortex filament method with the three most used reconnection criteria [22,32,51] and found which properties are strongly affected by the choice of the reconnection criteria (e.g., the reconnection rate differs more than in order of magnitude for different criteria), which properties only relatively weakly depend on this choice (such as mean properties of the tangle) and which are insensitive to it (such as probability distribution functions of local properties). Our results partially agree with preliminary observations by Baggaley [52] who recently compared the values of the vortex line density calculated with a number of reconnection criteria for $T = 1.6$ K and $0.35 < V_{ns} < 0.65$ cm/s and concluded that the values of $\mathcal{L}$ are insensitive to the choice of the criterion for these parameters.

The paper is organized as follows. In Sec. II, we describe mean and local statistical characteristics of vortex tangle, studied in the paper. Section III is devoted to a brief overview of the vortex filament method. In particular, in Sec. III A,

we present the basic equation of the vortex line motion. In Sec. III B, we discuss the reconnection criteria, and clarify in Sec. III C the implementation details.

Our results are presented and discussed in Secs. IV–VI. In Sec. IV, we consider the dynamics of the vortex tangle, including its evolution toward steady state and reconnection dynamics with different reconnection criteria. Here, we also show the typical tangle configurations for different reconnection criteria. In Sec. V, we describe the mean characteristics of vortex tangle, starting in Sec. V A with a detailed discussion of the vortex line density and its dependence on the temperature and counterflow velocity in comparison with results of other simulations and laboratory experiments. We also discuss the mean tangle anisotropy, the mean and root-mean-square (RMS) vortex line curvatures, the mean friction force between normal and superfluid components, the drift velocity of the vortex tangle, and the mean and most probable loop lengths. The central Sec. VI is devoted to the detailed microscopic description of the quantum vortex tangle in terms of PDFs and correlation functions. In particular, we have found that the core of the PDF of vortex loop lengths, Eq. (22), and the PDF of line curvature, Eq. (23), have an exponential form with a linear prefactor $[\propto x \exp(-x)]$, while the PDF of the mean-loop curvature has a Gaussian form, Eq. (25) $[\propto \exp(-x^2)]$. In addition, we demonstrate that the mean loop length essentially (more than by an order of magnitude) exceeds the most probable loop length because of the long tail of the corresponding PDF, which accumulates about 70–80% of the total probability. We also characterized the correlation between the length of the loops and their mean curvature and showed, in particular, that the mean radius of curvature of short loop is about their length divided by 2π, while that of the long loops is about the intervortex distance. Finally, we found the autocorrelation of the vortex line orientation, which decays at separations about the mean intervortex distance. These observations can be easily rationalized by understanding that the short loops are nearly circular, while the long loops may be approximated by random Gaussian ravel.

The concluding Sec. VII summarizes our view and results on the physical picture of ^{4}He counterflow turbulence. It begins in Sec. VII A with a short discussion of standard idealizations and their realizability that determine the set of relevant physical parameters of the problem. In Sec. VII B, employing dimensional reasoning and (where required) some simple physical arguments, we use the latter to describe the dependence of the basic physical characteristics of the problem on the counterflow velocity. Next, we present a detailed summary of our numerical results and list the actual numerical values of the corresponding dimensionless parameters which, according to naïve dimensional reasoning are expected to be of the order of unity.

In the short Sec. VII C, we recall relations that stem from the local induction approximation [19] that bridge the vortex line density, the mutual friction force, and the tangle drift velocity with the anisotropy and curvature parameters of the tangle. We summarize our results on the realizability of these relations in numerical simulation with the full Biot-Savart equations and conclude that although the local induction approximation to Eq. (12) fails to reproduce accurately the vortex tangle properties in numerical studies [22], we demonstrate that the analytical relationships between different mean characteristics of the vortex tangles, found in Ref. [19] within the LIA framework, are well-obeyed in our Biot-Savart similatons. Therefore we think that the local induction approximation may be effectively used in the analytical theory of counterflow turbulence.

In the next section, Sec. VII D, we summarize our results on various PDFs that characterize different aspects of the tangle statistics. The last, more technical section, Sec. VII E, overviews the dependence of our numerical results on the reconnection criteria showing that the vortex filament method in the framework of full Biot-Savart equation (12) provides an adequate qualitative and a reasonably accurate quantitative information on the quantum vortex dynamics in superfluid turbulence. This information is required for the further development of an adequate physical model of this intriguing phenomenon.

II. STATISTICAL DESCRIPTION OF THE VORTEX TANGLE

A. Statistical characteristics of the vortex tangle

1. Geometrical description of the vortex tangle

The geometry of the vortex tangle is presented in Fig. 1. We denote by $\boldsymbol{s}(\xi)$ a Cartesian coordinate of the vortex line, parameterized with the arc length ξ, by $\boldsymbol{s}'(\xi) \equiv d\boldsymbol{s}/d\xi$ a local direction of the vortex line, and by $\boldsymbol{s}''(\xi) \equiv d^2\boldsymbol{s}/d\xi^2$ a local curvature vector.

2. The vortex line density $\mathcal{L}$ and the parameter γ

Denote the total vortex length in the tangle occupying a volume $\mathcal{V}$ as $L_{\rm tot}$ and the length of particular j loop as l_j. Then the vortex line density (VLD) $\mathcal{L}$ and mean intervortex distance

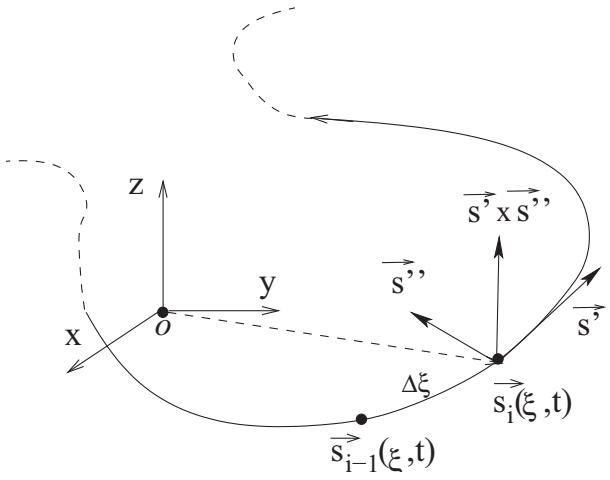

FIG. 1. The coordinate system. The origin of the Cartesian system is placed at the center of the computational box. Each vortex line point $\boldsymbol{s}_i$ is defined by Cartesian coordinates x_i, y_i, z_i, and a label ξ along the line. Vectors $\boldsymbol{s}'$, $\boldsymbol{s}''$, and $\boldsymbol{s}' \times \boldsymbol{s}''$ are the tangential, the local curvature vector and the direction of the local induced velocity, associated with the point $\boldsymbol{s}(\xi)$ of the vortex filament, respectively. Primes denote differentiation with respect to the instantaneous arc length ξ.

ℓ can be found as

$$L_{\rm tot} = \int_{\mathcal{C}} d\xi = \sum_{j=1}^{N} l_j, \quad \mathcal{L} \equiv L_{\rm tot}/\mathcal{V}, \quad \ell \equiv 1/\sqrt{\mathcal{L}}. \quad (1)$$

Here, N is the total number of loops and the integral is taken over the whole vortex configuration $\mathcal{C}$.

Asserting that κ ($[\kappa] = {\rm cm}^2/{\rm s}$) is the only relevant parameter in the problem and $[\mathcal{L}] = 1/{\rm cm}^{-2}$, one can employ the counterflow velocity $V_{\rm ns} \equiv V_{\rm n} - V_{\rm s}$ in a dimensional argument to write $\sqrt{\mathcal{L}} \sim V_{\rm ns}/\kappa$ or

$$\sqrt{\mathcal{L}} = \frac{\Gamma}{\kappa} V_{\rm ns}, \quad \gamma \equiv \frac{\Gamma}{\kappa}. \quad (2a)$$

Here, $V_{\rm n}$ and $V_{\rm s}$ are the mean normal and superfluid velocities and Γ is a dimensionless parameter, which in general is temperature dependent. Naïvely, one expects that Γ is of the order of unity. Numerical and experimental studies (see, e.g., our Table III) give $\Gamma \sim 0.1$.

It is customary to use in relation (2a) a dimensional parameter $\gamma(T)$ instead of Γ. The parameter γ is the subject of intensive experimental, numerical, and theoretical studies and will be discussed in details in Sec. V A.

In practice, most experimental and numerical data of the time averaged steady-state value of $\mathcal{L}$ are approximated by a slightly different form of this equation[13]:

$$\mathcal{L} = \gamma^2 (V_{\rm ns} - v_0)^2, \quad (2b)$$

which includes an additional fitting parameter, the intercept velocity v_0.

3. Reconnection dynamics and parameter $c_{\rm r}$

The reconnections between vortex lines lead to the development of a steady-state vortex tangle. The statistics of the reconnections is therefore important for characterizing the tangle. In a periodic box, only two kinds of reconnection are possible: one vortex loop splits into two smaller loops, or two loops merge into one larger loop. The ratio of the number of reconnections of two types (in a unit volume), N_1/N_2, is shown in Fig. 6.

The second important characteristic of the vortex dynamics is the total reconnection rate $dN_{\rm r}/dt$ ($N_{\rm r} \equiv N_1 + N_2$) in a unit volume. In the steady state, the relation between mean reconnection rate $\langle dN_{\rm r}\rangle/dt$ and $\mathcal{L}$ can be found by a simple dimensional argument: $[\langle dN_{\rm r}\rangle/dt] = {\rm cm}^{-3}{\rm s}^{-1}$ may be uniquely expressed via $[\kappa] = {\rm cm}^2/{\rm s}$ and $[\mathcal{L}] = {\rm cm}^{-2}$ as [48,53–55]

$$\frac{dN_r}{dt} = c_{\rm r} \kappa \mathcal{L}^{5/2}. \quad (3)$$

Here, $c_{\rm r}$ is a temperature dependent dimensionless coefficient. One sees in Fig. 7 that the relation (3) is perfectly obeyed in our simulations but the numerical values of $c_{\rm r}$, given in Table II, crucially depend on the reconnection criteria. The reasons and consequences of this fact for the final steady-state tangle are discussed in Sec. IV C.

4. Anisotropy of the vortex tangle and the indices $I_{\|}, I_{\perp}, I_{\ell}, I_{\ell\perp}$

The presence of the counterflow velocity creates a preferred direction and the vortex tangle is anisotropic. To measure the degree of anisotropy of the tangle, Schwarz [19] introduced the anisotropy indices:

$$I_{\|} = \frac{1}{L_{\rm tot}} \int_{\mathcal{C}} [1 - (\boldsymbol{s}' \cdot \hat{\boldsymbol{r}}_{\|})^2] d\xi, \quad (4a)$$

$$I_{\perp} = \frac{1}{L_{\rm tot}} \int_{\mathcal{C}} [1 - (\boldsymbol{s}' \cdot \hat{\boldsymbol{r}}_{\perp})^2] d\xi, \quad (4b)$$

$$I_{\ell} = \frac{\ell}{L_{\rm tot}} \int_{\mathcal{C}} \hat{\boldsymbol{r}}_{\|} \cdot (\boldsymbol{s}' \times \boldsymbol{s}'') d\xi, \quad (4c)$$

where $\hat{\boldsymbol{r}}_{\|}$ and $\hat{\boldsymbol{r}}_{\perp}$ are unit vectors in the direction parallel and perpendicular to $\boldsymbol{V}_{\rm ns}$, respectively. In the steady state, these indices averaged over time obey the relation $I_{\|}/2 + I_{\perp} = 1$. The index I_{ℓ} measures the mean local velocity (in unites κ/ℓ) in the direction of the counterflow. In the isotropic case, $I_{\|} = I_{\perp} = 2/3, I_{\ell} = 0$.

To test the isotropy of the velocity in the direction perpendicular of the counterflow, we also measure

$$I_{\ell\perp} = \frac{\ell}{L_{\rm tot}} \int_{\mathcal{C}} \hat{\boldsymbol{r}}_{\perp} \cdot (\boldsymbol{s}' \times \boldsymbol{s}'') d\xi, \quad (4d)$$

which is expected to vanish if the velocity is isotropic in the plane perpendicular to the counterflow velocity, even if I_{ℓ} is not small. Our results for the dimensionless anisotropy indices are given in Table IV and discussed in Sec. V B.

5. Mean, RMS curvatures $\overline{S}$ and $\widetilde{S}$, and parameters c_1 and c_2

Other important global properties of the vortex tangle are the mean and RMS curvatures $\overline{S}$ and $\widetilde{S}$, which may be expressed as an integral over the whole vortex configuration $\mathcal{C}$, occupying a volume $\mathcal{V}$:

$$\overline{S} \equiv \langle |s''| \rangle = \frac{1}{L_{\rm tot}} \int_{\mathcal{C}} |s''| d\xi, \quad (5a)$$

$$\widetilde{S}^2 \equiv \langle |s''|^2 \rangle = \frac{1}{L_{\rm tot}} \int_{\mathcal{C}} |s''|^2 d\xi. \quad (5b)$$

These objects are expected to scale with the mean density as [19]

$$\overline{S} = c_1 \sqrt{\mathcal{L}}, \quad \widetilde{S} = c_2 \sqrt{\mathcal{L}}, \quad (5c)$$

where c_1 and c_2 are dimensionless constants of the order of unity (see Table IV).

Similarly, we can find the mean and RMS curvature $\overline{s''_j}$ and $\widetilde{s''_j}$ of a particular vortex loop $\mathcal{C}_j$ of length $l_j \equiv \int_{\mathcal{C}_j} d\xi$:

$$\overline{s''_j} \equiv \langle |s''| \rangle_j = \frac{1}{l_j} \int_{\mathcal{C}_j} |s''| d\xi, \quad (6a)$$

$$\widetilde{s''_j}^2 \equiv \langle |s''|^2 \rangle_j = \frac{1}{l_j} \int_{\mathcal{C}_j} |s''|^2 d\xi. \quad (6b)$$

The global (over the entire tangle) PDF of $|s''|$ and the PDFs of the vortex-loop length, l_j, the mean-loop curvature, $\overline{s''_j}$ and

the correlations between l_j and $\widetilde{s''_j}$ are presented and discussed in Sec. VI.

6. Drift velocity of the vortex tangle V_{vt} and parameter C_{vt}

The drift velocity of the vortex tangle with respect to the superfluid rest frame is

$$\boldsymbol{V}_{vt} = \frac{1}{L_{tot}} \int_{\mathcal{C}} \frac{d\boldsymbol{s}(\xi)}{dt} d\xi - \boldsymbol{V}_s, \tag{7a}$$

where the velocity of the vortex line point $d\boldsymbol{s}(\xi)/dt$ is given below by Eq. (10b). It is natural to expect that $\boldsymbol{V}_{vt}$ is proportional to the counterflow velocity $\boldsymbol{V}_{ns}$ and to introduce a dimensionless parameter C_{vt} as their ratio:

$$\boldsymbol{V}_{vt} = C_{vt} \boldsymbol{V}_{ns}. \tag{7b}$$

The values of C_{vt} are discussed in Sec. V D.

7. Friction force density and the Gorter-Mellink constant

In discussions of the mechanical balance in superfluid turbulence, an important role is played by the mutual force density exerted by the normal fluid on the superfluid. It may be found from Eq. (10b) (the term proportional to α' vanishes by symmetry) [19]:

$$\boldsymbol{F}_{ns} = \rho_s \kappa \, \alpha \, J, \; J \equiv -\frac{1}{\mathcal{V}} \int_{\mathcal{C}} \boldsymbol{s}' \times [\boldsymbol{s}' \times (\boldsymbol{V}_{ns} - \boldsymbol{V}_{si})] d\xi. \tag{8a}$$

The integral J [with dimensions $[J] = 1/(\text{s cm})$] may be uniquely expressed via κ and V_{ns} as V_{ns}^3/κ^2. This leads to the dimensional estimate for F_{ns}:

$$F_{ns} = \frac{\alpha \rho_s}{\kappa} (C_f V_{ns})^3, \tag{8b}$$

with a dimensionless temperature dependent constant C_f. This agrees with the Gorter-Mellink [24] result that reads $F_{ns} \propto V_{ns}^3$:

$$F_{ns} = A_{GM} \rho_s \rho_n V_{ns}^3. \tag{8c}$$

Comparing Eqs. (8b) and (8c), one finds the relationship between C_f and the dimensional Gorter-Mellink constant A_{GM}:

$$A_{GM} = C_f^3 \frac{\widetilde{\alpha}}{\kappa \rho}, \quad \widetilde{\alpha} \equiv \alpha \rho / \rho_n. \tag{8d}$$

As is known, the density ρ of ^{4}He varies only weakly with the temperature in the relevant temperature range, while α varies rapidly. It increases six times as T grows from 1.3 to 1.9 K, see Table I. On the other hand, the temperature dependence of the parameter $\widetilde{\alpha}$, that actually governs the temperature dependence of A_{GM}, is much weaker than α. Further discussion of the friction force density is given below in Sec. V E.

8. Autocorrelation of the vortex orientations

To test the relative polarization of the vortex lines, we measure an orientation correlation function

$$K(\boldsymbol{r}_1 - \boldsymbol{r}_2) = \langle \boldsymbol{s}'(\boldsymbol{r}_1) \cdot \boldsymbol{s}'(\boldsymbol{r}_2) \rangle_{\mathcal{C}}, \tag{9}$$

where $\boldsymbol{r}_1$ and $\boldsymbol{r}_2$ are the Cartesian coordinates of the two line points and we average over all pairs of the line points in the tangle. $K(\boldsymbol{r}_1 - \boldsymbol{r}_2)$ measures the average angle between line segments as a function of the distance between them. Averaged over all distances it quantifies the polarization of the tangle $\overline{K}$.

TABLE I. Friction parameters α and α' used in simulations, relative density of the normal component [60], combination $\alpha\rho/\rho_n$ [which weakly depends temperature and is responsible for the mutual friction density in Eq. (8d)] and LIA parameter $\widetilde{\Lambda}$ calculated for $c = 1$.

T, K	1.3	1.6	1.9
α	0.036	0.098	0.210
α'	0.014	0.016	0.0009
ρ_n/ρ	0.045	0.162	0.420
$\alpha\rho/\rho_n$	0.8	0.6	0.5
$\widetilde{\Lambda} \equiv \Lambda/(4\pi)$	1.05	1.03	1.02

III. VORTEX FILAMENT METHOD

The vortex filament method and the reconnection criteria were presented in details, e.g., in Refs. [18–22,29,51,52,56]. Nevertheless, to keep the paper self-contained, and to introduce notations and definitions, we review these criteria with the focus on the underlying physical processes. The basic equations are presented in Sec. III A and the criteria of vortex reconnection are discussed in Sec. III B. A short description of the implementation details is given in Sec. III C.

A. Basic equations and their implementation

1. Equations of motion of the vortex line

When no external forces act on the vortex core the vortex line moves with the velocity $\boldsymbol{V}_{si}(\boldsymbol{s})$ defined by the entire vortex tangle according to the Biot-Savart equation:

$$\boldsymbol{V}_{si}(\boldsymbol{s}) = \frac{\kappa}{4\pi} \int_{\mathcal{C}} \frac{(\boldsymbol{s}_1 - \boldsymbol{s}) \times d\boldsymbol{s}_1}{|\boldsymbol{s}_1 - \boldsymbol{s}|^3}. \tag{10a}$$

Here, the vortex line is presented in a parametric form $s(\xi,t)$, where ξ is an arclength, t is the time, and the integral is taken over the entire vortex tangle configuration.

In addition to the self-induced velocity of the superfluid component, we have to account for the interaction with the normal component via mutual friction, characterized by two dimensionless temperature dependent parameters α and α' [18,19]:

$$\frac{d\boldsymbol{s}}{dt} = \boldsymbol{V}_s + \boldsymbol{V}_{si} + \alpha \boldsymbol{s}' \times (\boldsymbol{V}_{ns} - \boldsymbol{V}_{si}) - \alpha' \boldsymbol{s}' \times [\boldsymbol{s}' \times (\boldsymbol{V}_{ns} - \boldsymbol{V}_{si})] + \boldsymbol{v}_{bc}. \tag{10b}$$

Here, $\boldsymbol{V}_s$ is the macroscopic superfluid velocity, and the counterflow velocity $\boldsymbol{V}_{ns} = \boldsymbol{V}_n - \boldsymbol{V}_s$ is the relative velocity of the superfluid component. In the reference frame comoving with the superfluid component, $V_s = 0$ and the relative velocity equals to the velocity of normal fluid $\boldsymbol{V}_{ns} = \boldsymbol{V}_n$ in this reference frame. In our simulations, $\boldsymbol{V}_{ns}$ is oriented towards the positive z direction. The prime in $\boldsymbol{s}'$ denotes derivative with respect to the instantaneous arc length ξ, e.g., $\boldsymbol{s}' = d\boldsymbol{s}/d\xi$. The

mean velocities obey a mass conservation law $\rho_s \boldsymbol{V}_s + \rho_n \boldsymbol{V}_n = 0$, where ρ_n and ρ_s are the densities of normal and superfluid components, respectively. The density $\rho = \rho_n + \rho_s$ refers to the density of ^{4}He. The term $\boldsymbol{v}_{\rm bc}$ describes the influence of the boundary conditions. For the periodic boundary conditions used in this work, the line points leaving the box from one side were algorithmically brought back to the computational volume by appropriately shifting their coordinates without changing their velocity $\dot{\boldsymbol{s}}(z) = \dot{\boldsymbol{s}}(z + H)$, $\dot{\boldsymbol{s}}(y) = \dot{\boldsymbol{s}}(y + H)$, and $\dot{\boldsymbol{s}}(x) = \dot{\boldsymbol{s}}(x + H)$, where H is the size of the computational domain.

2. Local induction approximation

Equation (10a) implies that the vortex line is infinitely thin. Attempting to calculate the velocity at a particular point $\boldsymbol{s}$ on the vortex line, one finds that the integral logarithmically diverges as $\boldsymbol{s}_1 \to \boldsymbol{s}$. To resolve this difficulty, one has either to cut the integral at $|\boldsymbol{s}_1 - \boldsymbol{s}| = a_0$ or to account for the particular form of the vortex core structure. Physically, it means that $\boldsymbol{V}_{\rm si}(\boldsymbol{s})$ in the integral (10a) is dominated by the local contributions from the vortex line for which $a_0 \leqslant |\boldsymbol{s}_1 - \boldsymbol{s}| \leqslant cR$. The upper limit of integration is about the mean curvature of the tangle R determined up to a dimensionless constant c of the order of unity. Neglecting nonlocal contribution one arrives to the local induction approximation (LIA)[57,58]:

$$\boldsymbol{V}_{\rm si}^{\rm LIA} = \beta \boldsymbol{s}' \times \boldsymbol{s}'', \quad \beta \equiv \kappa \widetilde{\Lambda}, \quad \widetilde{\Lambda} \equiv \frac{\Lambda}{4\pi}, \tag{11a}$$

$$\Lambda = \ln\left(\frac{cR}{a_0}\right) \approx \ln\left(\frac{\ell}{a_0}\right). \tag{11b}$$

The value of the ratio of mean local to mean nonlocal contributions to the velocity is about Λ. Besides the traditional parameter Λ, we introduce also a frequently used combination $\widetilde{\Lambda}$. The values of $\widetilde{\Lambda}$ found numerically are very close to unity, see Table I.

Notice that Eq. (11a) is integrable, having an infinite number of integrals of motion, including the total line length. Therefore numerical simulations with the full BSE (10a) are not a question of accounting for a small (about 10%) nonlocal contributions to the line velocity but are required by necessity to account for the violation of infinitely many conservation laws.

Nevertheless one can exploit the fact that the local contribution (11a) to the vortex velocity does dominate the nonlocal one and to use the simple local relation (11a) in analytical studies of the vortex tangle characteristics, for example, in the way developed by Schwarz [19]. He established a set of bridge relations between different mean characteristics of the vortex tangle. In Secs. V A 4, V D, and V E, we demonstrate that these relations are well-obeyed by the mean vortex characteristics found directly from numerical simulations in the framework of the VFM with full Biot-Savart equations.

3. Implementation of the full Biot-Savart velocity

To implement the Biot-Savart equations in the vortex filament methods, we discretized the parametric curve by a large and variable number of points $s_i, i = 1, \ldots, N$ at initial space resolution $\Delta\xi$, see Fig 1. Then, the velocity of the point $\boldsymbol{s}$ is given by Eq. (10a) and desingularized according to Schwarz [18]:

$$\boldsymbol{V}_{\rm si}(\boldsymbol{s}) = \beta_{\rm VFM} \boldsymbol{s}' \times \boldsymbol{s}'' + \frac{\kappa}{4\pi} \int_{\mathcal{C}} \frac{(\boldsymbol{s}_1 - \boldsymbol{s}) \times d\boldsymbol{s}_1}{|\boldsymbol{s}_1 - \boldsymbol{s}|^3},$$
$$\beta_{\rm VFM} = \frac{\kappa}{4\pi} \ln\left(\frac{2\sqrt{l_+ l_-}}{e^{1/4} a_0}\right). \tag{12}$$

The integral accounts for the influence of the whole vortex configuration $\mathcal{C}$, excluding the segments adjacent to $\boldsymbol{s}$. Here, $\boldsymbol{s}_1$ is a the point on the filament. The contribution of the line elements adjacent to $\boldsymbol{s}$ is accounted for by the local term $\beta_{\rm VFM} \boldsymbol{s}' \times \boldsymbol{s}''$. Here, $l_\pm$ are the lengths of two line elements connected to $\boldsymbol{s}$, $e = 2.71\ldots$ is the base of natural logarithm and $e^{1/4}$ corresponds to the arbitrary chosen Rankine model of the vortex core [59].

The distances between adjacent line points change during evolution. The space resolution affects the accuracy of the derivatives $\boldsymbol{s}'$ and $\boldsymbol{s}''$ [56]. To keep $l_\pm$ of the same order of magnitude we remove a line point whenever two points come closer than $\Delta\xi_{\rm min}$ and add a point by a circular interpolation [19] if the distance between two adjacent points become larger than $\Delta\xi_{\rm max}$. Here, $\xi_{\rm min}$ and $\xi_{\rm max}$ are the chosen smallest and largest interpoint distances.

B. Criteria of vortex reconnection

In vortex filament methods, the reconnections are introduced algorithmically. When some criterion is satisfied, the vortex line topology is changed as shown in Fig. 2. These criteria are based on numerous studies of the vortex reconnections in the framework of the Biot-Savart and the Gross-Pitaevskii equations and on the resulting physical intuition.

1. Schwartz's geometrical criterion in LIA

Historically, the first criterion was suggested by Schwarz [18,19] in the context of the local induction approximation. He noticed that when two vortices approach each other closer than $2\ R/\Lambda$ [the distance at which the self-induced velocity, given by Eq. (11), is of the order of the nonlocal contribution] the vortex-vortex interaction dominates the local contribution, which in the framework of Eq. (10a) leads to a local instability. During this process, the velocity field of each vortex deforms the other in such a way that the vortices are moved toward each other and finally reconnect. Clearly, all this dynamics cannot be captured by the local induction approximation, which completely ignores the intervortex interactions. Thus Schwarz suggested a criterion that can be referred to as a "geometric criterion" for the local induction approximation, or LIA-GC: the vortices are reconnected when they approach each other closer than the minimal distance $\delta_{\rm LIA\text{-}GC}$:

$$\delta < \delta_{\rm LIA\text{-}GC} \equiv 2R/\Lambda, \tag{13}$$

i.e., the distance at which the nonlocal interactions exceed the local interactions.

2. Other geometric criteria for full Biot-Savart equations

In the framework of Biot-Savart equations, the LIA-GC criterion leads to many spurious reconnections. On the other

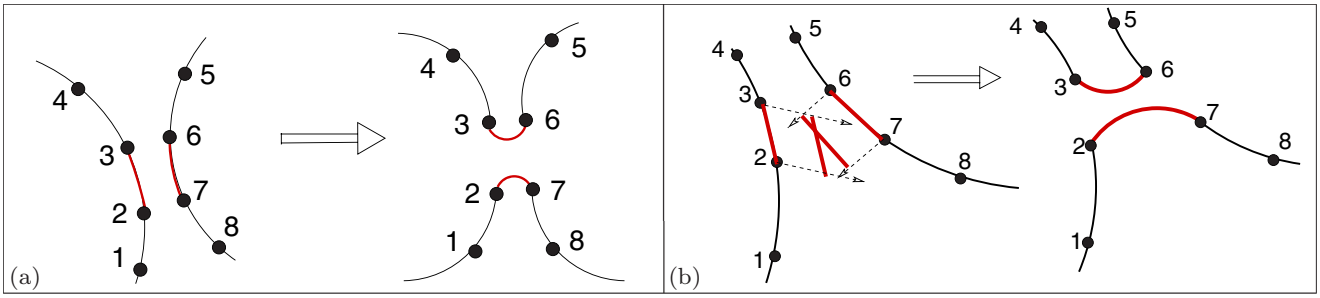

FIG. 2. (Color online) Topology change for the geometric (GC) and geometric-energetic reconnection criteria (GEC) (a) and dynamical reconnection criterion (DC) (b). The GC requires $l_{2,7} < \Delta\xi$ regardless the value of other distances, while GEC requires $l_{2,7} < \Delta\xi$ and, in addition, $l_{2,3} + l_{6,7} > l_{2,7} + l_{3,6}$. The DC requires that the segments (2,3) and (6,7), moving with constant speed, will cross in space during next time step.

hand, conceptually these equations provide an adequate description of the vortex dynamics in the reconnection processes up to the stage when $\delta \sim a_0$. Therefore the vortex filament method with the full Biot-Savart equations describes the vortex line motion for distances limited by its resolution $\delta > \Delta\xi$.

During the last decade, several reconnection criteria were proposed in which the closeness of the reconnecting points was related to the space resolution with or without additional physical requirements. Similar to Ref. [52], we consider here two such criteria.

A natural extension of LIA-GC (13) was suggested in Refs. [22,48]:

$$\delta < \delta_{\text{BSE-GC}} \simeq \Delta\xi. \tag{14}$$

By analogy with the LIA-GC criterion (13), we call this rule "BSE-geometrical criterion" (BSE-GC), see Fig. 2(a).

Unfortunately, the simple BSE-GC (14) ignores the energy dissipation during reconnection events, e.g., due to phonon emission. Since the vortex length approximates the kinetic energy of the tangle, it cannot increase during reconnections. A more restrictive criterion was suggested in Ref. [29], requiring a total vortex line length reduction in addition to the geometrical proximity, see Eq. (14). We will refer to this criterion as to the Biot-Savart equation (BSE) "geometric-energetic" criterion (BSE-GEC). In the present work, we deal only with full Biot-Savart simulations and therefore we skip hereafter the notation "BSE-" from the reconnection names and abbreviate them shortly as GC and GEC (or G criterion and GE criterion).

3. *Dynamical criterion*

The authors of Refs. [49–51] approached the problem of reconnection criterion completely differently, by considering the dynamics of vortex line points. Their approach is equally applicable to the local induction approximation as well as the Biot-Davart dynamics. Under the assumption that both ends of a line segment are moving at the same velocity during a time step, the reconnection is carried out if the reconnecting line segments cross in space during the next time step. We will refer to this criterion as the "dynamical" criterion (DC or D criterion). Note that unlike GC and GEC, the DC involves reconnecting segments and not points. The assumption of the same velocity of the two ends of a segment implies sufficiently high space resolution (small values of $\Delta\xi$), see Fig. 2(b).

To find whether the line segments will meet during the next time step, the set of equations

$$\boldsymbol{s}_i + V(\boldsymbol{s}_i)\tau + (\boldsymbol{s}_{i+1} - \boldsymbol{s}_i)\theta = \boldsymbol{s}_j + V(\boldsymbol{s}_j)\tau + (\boldsymbol{s}_{j+1} - \boldsymbol{s}_j)\phi \tag{15}$$

is solved for $0 \leqslant \theta \leqslant 1$, $0 \leqslant \phi \leqslant 1$, and $0 \leqslant \tau \leqslant \Delta t$. If such a solution is found, the segments will collide. Here, $\boldsymbol{s}_i = (x_i, y_i, z_i)$, $\boldsymbol{s}_{i+1} = (x_{i+1}, y_{i+1}, z_{i+1})$ and $\boldsymbol{s}_j = (x_j, y_j, z_j)$, $\boldsymbol{s}_{j+1} = (x_{j+1}, y_{j+1}, z_{j+1})$ (in Cartesian coordinates) denote the first and the second reconnecting pairs of points and Δt is the time step. The velocities $V(\boldsymbol{s}_i)$ and $V(\boldsymbol{s}_j)$ remain the velocities of the line points $\boldsymbol{s}_i$ and $\boldsymbol{s}_j$. Alternatively, the velocities of the midpoint of the segments $(i, i+1)$ and $(j, j+1)$ may be used.

C. Implementation details

The simulations were carried out in the cubic box $H = 0.1$ cm for temperatures $T = 1.3$, 1.6, and 1.9 K and counterflow velocities V_{ns} from 0.3 to 1.2 cm/s. The parameters α and α' are given in Table I. The initial condition consisted of 20 circular rings of radius $R_0 = 9 \times 10^{-3}$ cm oriented such that the total momentum of the system vanished. The radius of the rings was chosen to exceed the critical radius of the surviving loop[18,20] $R_{\text{cr}} \approx 3 \times 10^{-3}$ cm for the weakest thermal flow ($T = 1.3$ K, $V_{\text{ns}} = 0.3$ cm/s).

The initial space resolution $\Delta\xi = 8 \times 10^{-4}$ cm for D criterion and 1.6×10^{-3} cm for GC and GEC was used. At these values, the results were insensitive to the resolution as was verified by simulations with larger and smaller values of $\Delta\xi$. As it was mentioned above, the line points were removed or added during evolution to keep $\Delta\xi/1.8 \leqslant l_{\pm} \leqslant 1.8\Delta\xi$.

We use the fourth-order Runge Kutta method for the time marching with the time step related by the stability condition to the line resolution. For simulations with GC and GEC $\Delta t = 3.8 \times 10^{-4}$ s, while for DC, $\Delta t = 9.5 \times 10^{-5}$ s was used. The time evolution was followed for 150 seconds for GC and GEC and for 75 seconds for DC.

The directionality of the vortex lines is conserved during the reconnection procedure. The candidate points for reconnections are sought within $1.1\Delta\xi$ distance for GC and GEC

and within the distance defined by a maximum velocity in the tangle at the reconnection time $2\Delta t\, V_{\max}$ for DC. Note that in Ref. [52], the candidate pairs for similar criterion were sought within distance $\Delta\xi$.

Similar to Ref. [22], we remove the small loops and loop fragments with three or less line segments that are expected to disappear due to the mutual friction. The maximum length of the removed loops is 8.6×10^{-3} cm for DC and 1.7×10^{-2} cm for GC and GEC, which is smaller than the length of the loop of the critical size 1.88×10^{-2} cm. This procedure was applied in all simulations.

An additional requirement that the angle between reconnecting segments is at least 10° [$\cos(\boldsymbol{s}_i, \boldsymbol{s}_j) < 0.9848$], applied to GEC, was introduced similar to Ref. [52]. We performed simulations without this additional requirement as well and did not find any difference in the results.

In BSE simulations under periodic boundary conditions, a particular care should be taken in calculation of the nonlocal part of the velocity. The line points, that are separated by the size of the computational box due the periodic boundary conditions, are in fact nearest neighbors for the calculation of the Biot-Savart integral. To account for the influence of every filament of the tangle at a proper distance, the main computational domain is surrounded by 26 replicas. The contribution of the distant filaments falls off quickly with increasing distance. We have verified that in our simulations the influence of the replica domains touching the cube edges and corners is negligible. The influence of the replica domains bordering the faces of the main domain was studied and discussed below. All results below are calculated using only the main computation domain. We should stress, however, that this approximation is valid only when the vortex tangles are not very dense and the vortex lines are highly curved (as in the counterflow). In this case, the local contribution to the velocity field dominates the nonlocal. This may not be the true in other systems. For example, in quasiclassical systems, the vortices are expected to form bundles, and here the nonlocal contribution will be more important. Therefore the one-domain approximation should be tested in any computational setting to ensure that the Biot-Savart integral is calculated properly and periodic wrapping can be safely neglected.

At each time step, we propagate the line points, adjust the space resolution, perform the reconnections, remove small loops and then adjust the resolution again. Unlike Ref. [52], we reconnect all pairs of points and segments that satisfy the reconnection criterion, and not just the closest ones. This may lead to slightly larger number of reconnection than in Ref. [52].

IV. DYNAMICS OF THE VORTEX TANGLE

A. Evolution of the tangle toward steady state

A typical time evolution of the vortex tangle is shown in Fig. 3. Panel *A* illustrates that the steady state is independent of the initial conditions: the evolution at $T = 1.6$ K and $V_{\rm ns} = 1$ cm/s, started from the 20-ring configuration (blue solid line) as well as from the steady state configurations for $T = 1.3$ and 1.9 K, (green dashed and red dot-dashed lines, respectively) all give the same steady-state vortex line density. This (expected) result allows us to perform all the simulations starting from the same simple 20-ring configuration.

As one sees in Fig. 3(a), the transient time $\tau_{\rm tr}$ it took for the initial configuration to reach the steady state is the shortest for the most dense initial configuration (steady state at $T = 1.9$ K, red dashed line) and the longest for the most sparse one (20-rings, blue solid line). This can be easily rationalized by a dimensional reasoning according to which

$$\tau_{\rm tr} \sim 1/(\kappa\, \mathcal{L}) = \ell^2/\kappa. \tag{16}$$

This dependence also agrees with our observations that $\tau_{\rm tr}$ is longer for low temperatures (for which the resulting $\mathcal{L}$ is smaller), and shorter for large T, at which the tangle is more dense. For moderate values of $\mathcal{L} \simeq 3 \times 10^3$ cm^{-2} the estimate (16) gives $\tau_{\rm tr} \sim 0.3$ s. This is slightly shorter than the values observed numerically.

The values of $\tau_{\rm tr}$, deduced from Fig. 3(a), agree surprisingly well with the experimental results of Vinen [10] [see Fig. 2(d)] for $T = 1.6$ K. At this temperature, the transient time decreases continuously with the inscreasing amount of initially present turbulence. When helium was not excited initially, the time to reach the steady state was about 1.9 s. It decreased

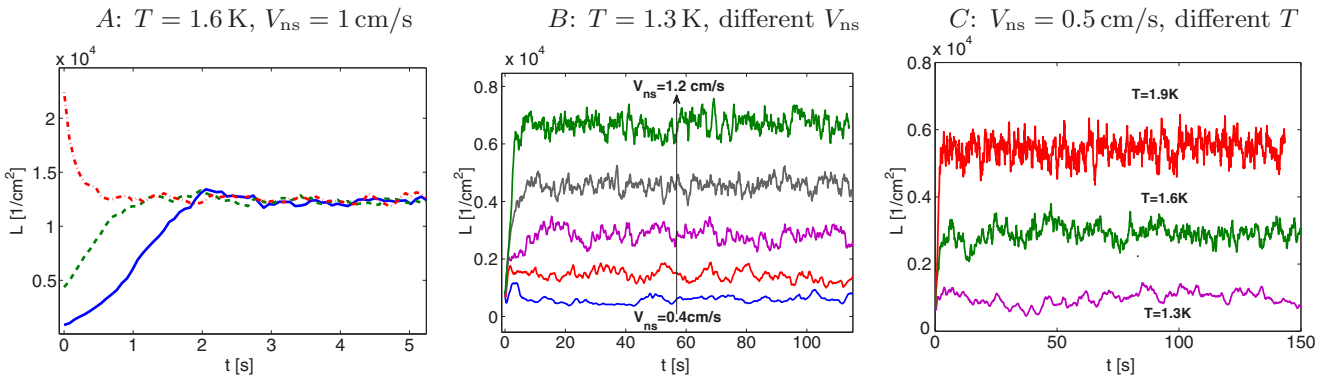

FIG. 3. (Color online) (a) Transient regime (with GEC) started from 20-ring configuration (blue solid line), from the steady-state configuration obtained at $T = 1.3$ K and $V_{\rm ns} = 1$ cm/c (green dashed line) and from the steady-state configuration obtained at $T = 1.9$ K and $V_{\rm ns} = 1$ cm/c (red dot-dashed line). (b) VLD evolution $T = 1.3$ K for counterflow velocities 0.4, 0.6, 0.8, 1.0, and 1.2 cm/s (from bottom to top). (c) VLD evolution for different temperatures and $V_{\rm ns} = 0.5$ cm/s.

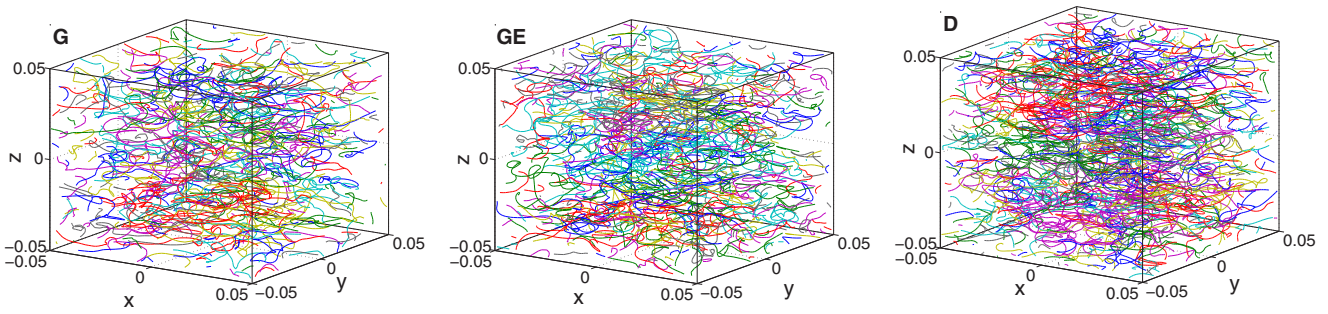

FIG. 4. (Color online) Typical tangle configurations for different reconnection criteria at $T = 1.9$ K and $V_{ns} = 1$ cm/s. Different loops are marked by different colors for clarity.

to about 1 s for moderately excited and to less than 0.5 s for strongly excited helium, similar to our results.

Another important characteristic of the vortex dynamics, clearly seen in Figs. 3(b) and 3(c), is the large amplitude of fluctuations in density in the steady state, which reach up to 12% of the steady-state vortex line density for weak counterflow velocities. One sees also that the mean line density increases both with V_{ns} and temperature, such that the same line density may be obtained at lower temperatures and stronger counterflow velocity or at higher T and smaller V_{ns}.

B. Tangle visualization and intervortex distance

The typical dense steady-state tangles obtained with different reconnection criteria are shown in Fig. 4 for $T = 1.9$ K and $V_{ns} = 1$ cm/s. At these parameters the difference in density is visible to the naked eye: the most dense tangle is obtained with DC and the most sparse with GC. An important characteristic of the developed tangle is the intervortex distance ℓ that quantifies the typical distance between the vortex lines. As seen from Fig. 5, the vortex lines come closer with increasing both counterflow velocity and temperature and ℓ becomes comparable with the space resolution $\Delta\xi$ at $T = 1.9$ K and the largest V_{ns} used in our simulations.

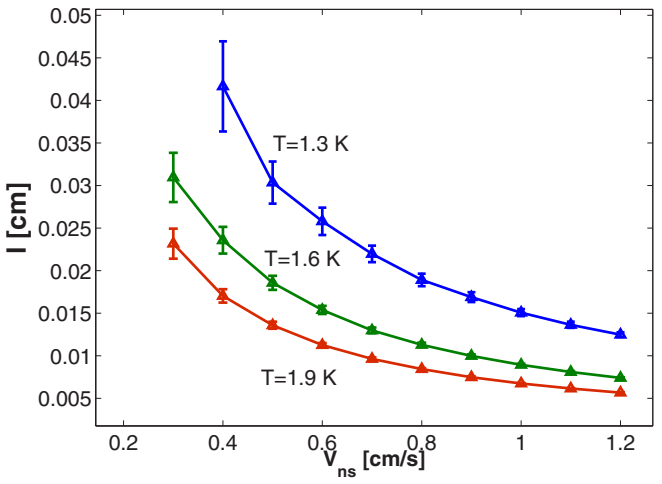

FIG. 5. (Color online) The intervortex distance $\ell = \mathcal{L}^{-1/2}$ as a function of V_{ns} for different temperatures (with GEC).

C. Reconnection dynamics

As said above, periodic boundary conditions allow only two types of reconnections: the merging of two loops into one ($2 \to 1$) and one loop splitting into two ($1 \to 2$). We denote below the reconnection rate per unit volume of the first type as N_1 and of the second type as N_2 and plot the ratio N_1/N_2 as a function of V_{ns}^2 in Fig. 6 for different conditions. The reconnections leading to splitting one loop into two are more frequent in all cases. For GC, the ratio is almost independent of V_{ns} and the merging of loops is even less frequent at $T = 1.9$ K. For DC, the ratio is temperature independent, but the first type of reconnection becomes more frequent with increasing V_{ns}. For GEC, the loops merging becomes less frequent with increasing both the temperature and the counterflow velocity. On the average only about 35–45% of reconnections lead to loops merging.

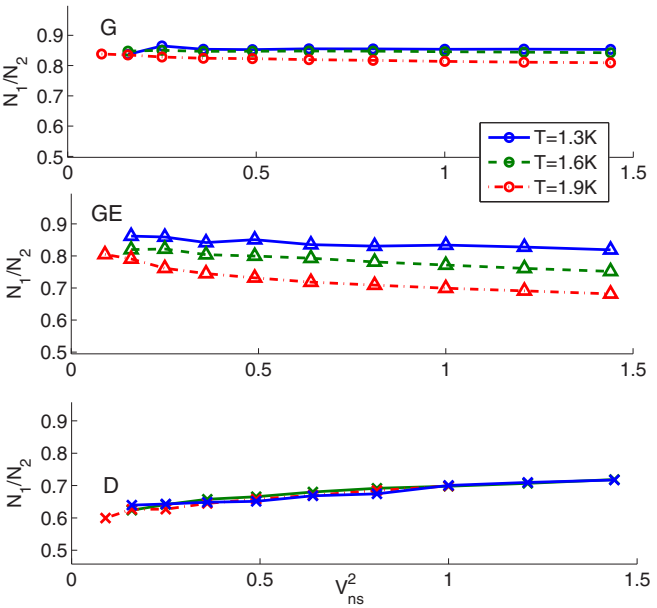

FIG. 6. (Color online) Ratio of reconnection rates of two types for different conditions. Circles denote DC, up-triangles are GEC, and crosses are DC. Solid lines correspond to $T = 1.3$ K, dashed lines to $T = 1.6$ K and dot-dashed lines to $T = 1.9$ K. Lines serve to guide the eye only.

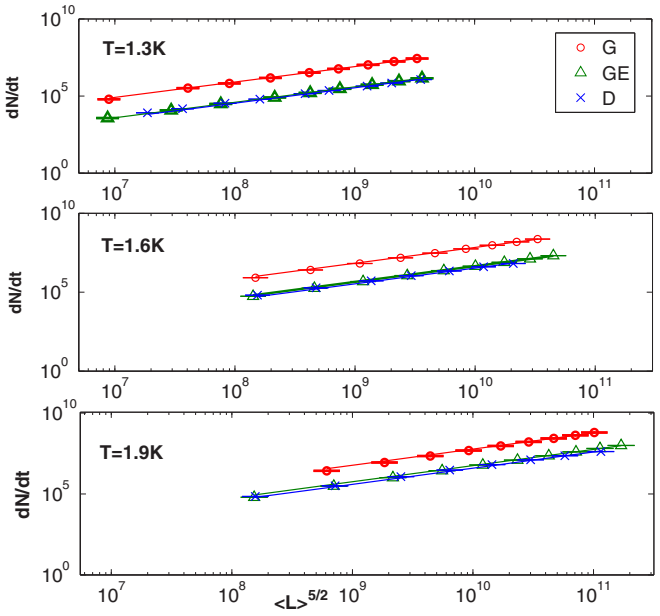

FIG. 7. (Color online) The mean reconnection rate dN_r/dt as a function of $\mathcal{L}^{5/2}$. The symbols with error bars are data, the lines are linear fit according to Eq. (3) (the fit passes through $\mathcal{L}^{5/2} = 0$).

In Fig. 7, we show the mean reconnection rate dN_r/dt as a function of $\mathcal{L}^{5/2}$. One sees that the linear relation (3) is well obeyed throughout the parameter range and for all three criteria of reconnections. The values of the coefficient c_r are given in Table II. Note that for all temperatures the reconnection rate for GC is several times higher than for GEC and DC, which are close to each other and their scaling coefficients fall within the range $0.1 < c_r < 0.5$, as predicted by Nemirovskii [54]. The much larger number of reconnections for GC is in agreement with the results of Baggaley [52] who found that the time between reconnections for this criterion was much shorter than for GEC. We conclude that geometric-energetic and dynamic criteria give reliable values of the reconnection rates, while a pure geometric criterion overestimates it by an order of magnitude.

Previously, the scaling coefficient c_r was calculated in Refs. [50,51] using DC within the local induction approximation. They found $c_r = 2.47$ for $T = 1.6$ K and $V_{ns} = 6$, 8, and 12 cm/s. This is much larger than our current result. The counterflow velocity in their case was much stronger than we use, and their vortex line density was also much larger. Thus the difference may stem from the usage of the local induction approximation, which is doubtful for these values of $\mathcal{L}$.

TABLE II. The reconnection rate scaling coefficient. The error bars were calculated from standard deviations of $dN_r/dt(t)$ and $\mathcal{L}$.

	Recon. crit.	$T = 1.3$ K	$T = 1.6$ K	$T = 1.9$ K
c_r	GC	8.0 ± 1.0	6.80 ± 0.5	6.0 ± 0.3
	GEC	0.39 ± 0.05	0.45 ± 0.03	0.57 ± 0.03
	DC	0.34 ± 0.05	0.34 ± 0.03	0.40 ± 0.13

V. MEAN CHARACTERISTICS OF THE TANGLE

A. Vortex line density $\mathcal{L}$

1. Numerical results for $\mathcal{L}$ versus counterflow velocity

The steady-state value of $\mathcal{L}$ was obtained by averaging $\mathcal{L}(t)$ over the plateau values for 10–150 s for $T = 1.3$ K and for 5–150 s for $T = 1.6$ and 1.9 K for GC and GEC and up to 75 s for DC. The error bars in the figures were calculated by the standard deviation over the same time period. In Fig. 8, we present $\mathcal{L}$ as a function of the counterflow velocity and the fit according to Eq. (2b). Clearly, the data follow this linear relation faithfully and the corresponding γ and v_0 are given in Table III. A measurable difference between the results with only the main computational domain and with additional six replicas touching its faces was found only for $T = 1.9$ K and $V_{ns} > 0.5$ cm/s, resulting in $\gamma = (146.2 \pm 0.2)$ s/cm^2 compared to $\gamma = (148.0 \pm 0.2)$ s/cm^2 (for GE criterion) for the main domain (about 1% difference). Similar corrections were obtained for the other criteria. We therefore conclude that for the parameter range used in our work it is sufficient to calculate the Biot-Savart velocities in the main domain only.

The values of γ, which were calculated in Ref. [52], were obtained for counterflow velocities $0.35 < V_{ns} < 0.6$ cm/s at $T = 1.6$ K, while in Ref. [22] a similar range of $V_{ns} < 0.6$ cm/s was used for $T = 1.9$ K. For these parameters, we found that the difference in the computed value of $\mathcal{L}$ for different reconnection criteria was relatively small. Our simulations with a wider range of counterflow velocities demonstrate that the values of $\mathcal{L}$ for three reconnection criteria are close only for $T = 1.3$ K, while for $T = 1.6$ and 1.9 K, they progressively deviate from each other, leading to different values of γ, see Fig. 8 and Table III. Quantifying the spread of the values as a difference between the largest and the smallest γ at each temperature divided by the mean value, we get about 7% for $T = 1.3$ K, about 13% for $T = 1.6$ K and about 28% for $T = 1.9$ K.

2. Comparison of numerical and experimental results

In Fig. 9, we compare the values of γ obtained in simulations with the experimental results. This is an issue that requires careful analysis of particular experimental conditions including the dependence on the channel width, the roughness of the walls, the finite value of the temperature difference with respect to the mean temperature, and problems with temperature stabilization.

Additional uncertainty arises from the fact that the thermal counterflow turbulence in square channels of width smaller than 1 mm may exist in two turbulent regimes[13]. The regime TI immediately follows the laminar state. The regime TII is found above some critical line density, usually at higher counterflow velocities. In both regimes, $\mathcal{L}^{1/2} = \gamma(V_{ns} - v_0)$ with γ in TII state larger than that in TI.

All these problems lead to a wide spread of experimental values of γ, see lines 1, 2, 3, 4 in Fig. 9. The values of γ for pure superflow (thin lines with open symbols, lines 1 and 2) are significantly larger than those for counterflows in TI state (thin lines with filled symbols, lines 3 and 4). As was discussed in Ref. [17], the values of γ in superflows are close to the results of counterflow in TII state.

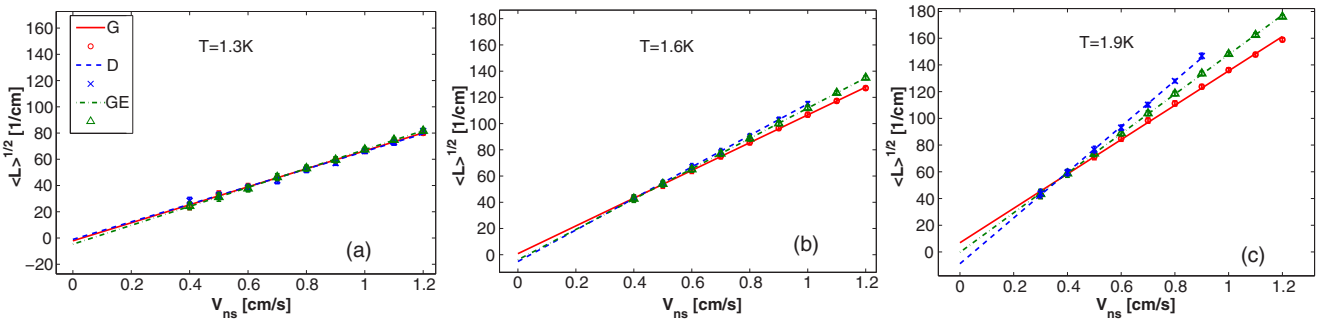

FIG. 8. (Color online) $\sqrt{\mathcal{L}}$ as a function of $V_{\rm ns}$ for (a) $T = 1.3$, (b) 1.6, and (c) 1.9 K. Symbols with error bars are the numerical results, lines are fits according to Eq. (2b). Three sets of symbols and lines correspond to different reconnection criteria as shown in the legend in (a).

Ignoring these differences in the experimental conditions, we note that (i) the spread of numerical results (ours and from Ref. [22]) is smaller than that of the experimental data and (ii) the numerical results lie within the spread of experimental values of γ. More experimental work is needed to better measure the values of γ and more numerical simulations are required to account, for example, for the boundary conditions with strong vortex pinning and laminar velocity profile of the normal components, which is not expected to be a constant even for pure superflow. Nevertheless, numerical and experimental results demonstrate qualitatively the same kind of behavior that allows us to hope that the main characteristics of turbulent counterflow are adequately reflected in the numerical simulations.

3. *Dependence of numerical results for vortex line density on reconnection criteria*

As we showed above, the values of γ for three different reconnection criteria increasingly differ with increasing temperature. These differences may be related to larger values of $\mathcal{L}$, i.e., to smaller intervortex distance $\ell = 1/\sqrt{\mathcal{L}}$. A possible explanation is that the vortex filament method with any reconnection criterion deteriorates when ℓ approaches the interpoint distance $\Delta\xi$, but the degree to which the dynamics of the tangle is affected depends on the reconnection criterion. We performed several control simulations with higher $V_{\rm ns}$ (not shown). Simulations at $T = 1.3$ K and $V_{\rm ns} = 2$ cm/s resulted in $\mathcal{L}$ similar to that for $T = 1.9$ K and $V_{\rm ns} = 0.9$ cm/s and followed the same line as all other results for $T = 1.3$ K. On the other hand, at $T = 1.9$ K and $V_{\rm ns} = 2$ cm/s, $\Delta\xi \approx \ell$ and the value of $\mathcal{L}$ was strongly underestimated. In all our simulations, the ratio $\Delta\xi/\ell \leqslant 0.2$ and we have checked that with twice larger ratio we got practically the same results.

We should stress that the steady state value of $\mathcal{L}$ is a result of a delicate balance of all the dynamical processes that are effected by the reconnections, explicitly and implicitly, via details of the resulting tangle characteristics. The final steady-state value of $\mathcal{L}$ may be counterintuitive. For instance, there

TABLE III. The values of γ (in s/cm^2) and $10^2 v_0$ (in cm/s) obtained from Eq. (2b) and approximate values of $\Gamma \equiv \gamma\kappa$ for GE criterion. The error bars for γ and v_0 were calculated from the standard deviation of $\mathcal{L}$ by textbook relations [61]. The values of γ from numerical simulations of Refs. [22,52], from Eq. (18) and the estimate (19) with $c_{\rm L}$ from Ref. [19] are given for comparison.

	Recon. criterion	$T = 1.3$ K	$T = 1.6$ K	$T = 1.9$ K
	GC	68.6 ± 0.1	105.8 ± 0.2	128.6 ± 0.7
γ, s/cm^2	GEC	72.1 ± 0.2	115.7 ± 0.1	148.0 ± 0.2
	DC	67.1 ± 0.4	120.2 ± 0.7	171.2 ± 2.6
$\Gamma \simeq$	GEC	0.07	0.12	0.15
	GC	3.1 ± 0.1	-0.8 ± 0.1	-5.4 ± 0.3
$10^2 v_0$, cm/s	GEC	6.6 ± 0.3	3.3 ± 0.1	0.2 ± 0.1
	DC	1.6 ± 0.4	4.3 ± 0.5	4.3 ± 0.4
γ, Ref. [22]	GC	53.1	109.6	140.1
	GC		116.9	
γ, Ref. [52]	GE		114.35	
	DC		112.3	
$\gamma_{\rm v}$, Eq. (18)		82	151	266
$\gamma_{\rm s}$, Eq. (19)	Ref. [19]	80	130	198

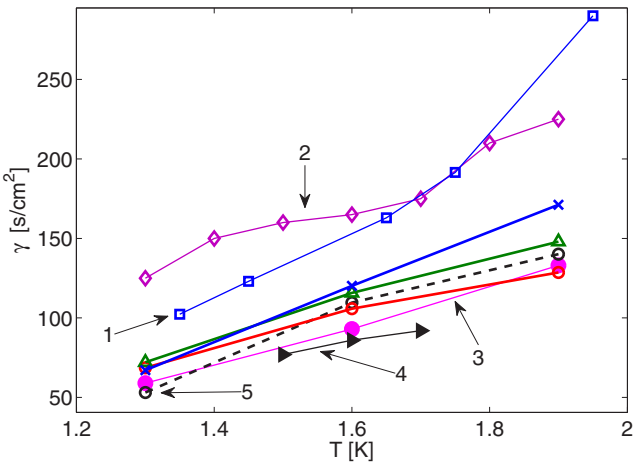

FIG. 9. (Color online) The numerical and experimental values of the parameter $\gamma(T)$. Thick solid lines with open symbols, marked with letters D (blue line with crosses), GE (green line with up-triangles), and G (red line with circles) are the results of our simulations with different reconnection criteria (DC, GEC, and GC, respectively). Line 5, black open circles with dashed line are the simulations of Adachi *et al.* [22], G criterion. Thin lines with open symbols are the results of experiments in pure superflow: (line 1) Babuin *et al.* [17], 7 × 7-mm channel and (line 2) Ashton *et al.* [23], 0.13-mm diameter glass channel. Thin lines with filled symbols are the results of experiments in counterflow: (line 3) Childers and Tough[12], TI state, 0.13-mm diameter glass channels and (line 4) Martin and Tough [62], TI state, 1-mm diameter glass channel.

exists an apparent contradiction: the only difference between GC and GEC is that in GC the reconnections increasing the length of the vortex line are allowed. Given a much larger number of reconnections in this case, one expects that the vortex line density should be larger for GC than for GEC, while in fact it is smaller. To resolve this contradiction, we analyzed the change in the length of the vortex tangle during transient evolution, before the steady-state tangle was formed. It turns out that the reconnection procedure for GC produce a large number of small loops and loops fragments with a number of segments not exceeding three. The number of these small loops increases as the tangle develops. Since in our procedure such small loops are removed from the configuration only after all the reconnections were made, only truly separate loops that did not merge back into larger loops are removed. The number of such small loops in GEC is about 10 times smaller, while with DC they are hardly created at all. Removal of these small rings slows down the growth of the length of the vortex tangle, in particular for GC, and results in smaller steady-state vortex line density in this case. For DC, on the other hand, no such mechanism exists and the vortex line density grows more before reaching the steady-state value.

In the developed tangle, the total length change due to reconnections, small loops removal and remeshing is small compared to the total line length and in a self-consistent manner helps to maintain the density of the tangle around its steady state value. At this stage, the difference between the reconnection criteria is not significant.

4. *Phenomenological analysis of $\gamma(T)$*

The naïve dimensional estimate $\Gamma \sim 1$ gives $\gamma \sim 1000\ \mathrm{s/cm^2}$. Much better estimates were obtained by using macroscopic properties of the vortex tangle.

In 1957 Vinen [9], suggested a phenomenological evolution equation for the $\mathcal{L}$:

$$\frac{d\mathcal{L}(t)}{dt} = \frac{\chi_1 B \rho_n \mathcal{L}^{3/2}}{2\,\rho}|V_{\rm ns}| - \frac{\chi_2 \kappa \mathcal{L}^2}{2\pi}. \tag{17}$$

It includes the vortex generation and vortex decay terms on its right-hand side (RHS). Here, $B(T)$ is the Hall-Vinen temperature dependent dimensionless coefficient, describing the interaction between the line and the normal fluid, while $\chi_1(T)$ and $\chi_2(T)$ are additional dimensionless phenomenological parameters. In the steady state, Eq. (17) results in the relation (2a) with

$$\gamma_{\rm v} = \frac{\pi B \rho_n \chi_1}{\kappa \rho \chi_2}. \tag{18}$$

Estimates of the coefficient $\gamma_{\rm v}$ with experimental values for B (for $V_{\rm ns} = 1\mathrm{cm/s}$) and χ_1, χ_2 [9,12,60] are shown in Table III. These values are close to the experimental γ measured in superflow[17,23].

Another estimate was obtained by Schwarz [19], who derived the equation of motion for the line density similar to Vinen's equation (17) from local induction approximation and balanced in the steady-state tangle the mean anisotropy of the self-induced velocity $\boldsymbol{s}' \times \boldsymbol{s}''$ in the Eq. (11) against its magnitude:

$$\gamma_{\rm s} = c_{\rm L}/\beta, \quad c_{\rm L} \equiv I_\ell / c_2^2. \tag{19}$$

TABLE IV. Anisotropy indices and mean curvature scaling coefficients. The values and error bars for anisotropy indices are the time averages (same time interval as for $\mathcal{L}$) and the standard deviation over the same period of time, respectively. The error bars for c_1 and c_2 were calculated from standard deviations of $|s''|$ and $|s''|^2$.

	Recon. criterion	$T = 1.3$ K	$T = 1.6$ K	$T = 1.9$ K
	GC	0.73 ± 0.03	0.76 ± 0.02	0.80 ± 0.01
$I_{\|\|}$	GEC	0.73 ± 0.03	0.76 ± 0.02	0.81 ± 0.01
Eq. (4a)	DC	0.74 ± 0.03	0.77 ± 0.02	0.82 ± 0.02
	GC	0.86 ± 0.06	0.81 ± 0.04	0.74 ± 0.02
$I_\perp/I_{\|\|}$	GEC	0.86 ± 0.05	0.80 ± 0.03	0.72 ± 0.02
Eq. (4b)	DC	0.85 ± 0.07	0.79 ± 0.03	0.71 ± 0.02
	GC	0.50 ± 0.09	0.52 ± 0.02	0.53 ± 0.03
I_ℓ	GEC	0.50 ± 0.08	0.53 ± 0.03	0.54 ± 0.02
Eq. (4c)	DC	0.51 ± 0.09	0.53 ± 0.03	0.52 ± 0.02
$I_{\|\|}$	GC [22]	0.738	0.771	0.820
$I_\perp/I_{\|\|}$	exp [11].	0.85 ± 0.05	0.8 ± 0.1	0.7 ± 0.1
	GC	2.26 ± 0.01	1.85 ± 0.003	1.68 ± 0.002
c_1	GEC	2.09 ± 0.01	1.68 ± 0.003	1.48 ± 0.001
Eq. (5c)	DC	2.28 ± 0.01	1.64 ± 0.003	1.48 ± 0.004
	GC	2.70 ± 0.10	2.19 ± 0.05	1.96 ± 0.03
c_2	GEC	2.60 ± 0.10	2.04 ± 0.04	1.78 ± 0.02
Eq. (5c)	DC	2.80 ± 0.20	2.11 ± 0.05	1.90 ± 0.07

Recall that $\beta = \kappa \widetilde{\Lambda}$ and the values of $\widetilde{\Lambda}$ are very close to unity, such that $\gamma_{\rm s} \approx 10^3 c_{\rm L}$.

The parameter $c_{\rm L}$, relating the $V_{\rm ns}$ dependence of $\mathcal{L}$ to the tangle anisotropy and RMS curvature, is one of the most important parameters of Schwarz's theory [19]. It defines, among other properties, the tangle drift velocity and the mutual friction force, discussed later in Secs. V D and V E. We can calculate $c_{\rm L}$, using I_ℓ and c_2 given in Table IV, and see how well the theory based on the local induction approximation works for the vortex tangles, obtained with full Biot-Savart simulations.

As we discuss in Secs. V B and V C, the anisotropy index I_ℓ is almost independent of both the temperature and the reconnection criterion, while c_2 changes with T and is different for different reconnection criteria. Therefore the T dependence of $c_{\rm L}$ (and consequently, that of $\gamma_{\rm s}$) is defined by the RMS curvature scaling coefficient c_2.

In Fig. 10, we show the parameter $c_{\rm L}$ for three reconnection criteria and the results of Schwarz [19], obtained with local induction approximation simulations. The overall trend is very similar to that of γ, shown in Fig. 9, except that in this case it is the GE criterion that gives the largest values and not DC, as for γ. As could be expected, the results for the three criteria differ most at $T = 1.9$ K and the estimates for $\gamma_{\rm s} \approx 10^3 c_{\rm L}$ give values slightly larger than γ, see Table III. The values of $c_{\rm L}$, obtained by Schwarz from the local induction approximation simulations, are even larger. We therefore conclude that the nonlocal corrections to the line velocity affect the mean tangle properties by decreasing the vortex line density for stronger counterflow velocities.

Schwarz [19] also related the phenomenological coefficients χ_1 and χ_2 to the properties of the steady-state tangle as $\chi_1 = I_\ell, \chi_2 = 2\pi\alpha\beta I_\ell/\kappa c_{\rm L}$. Indeed, substituting these definitions to Eq. (18) and recalling that $\alpha = B\rho_n/2\rho$, we find that

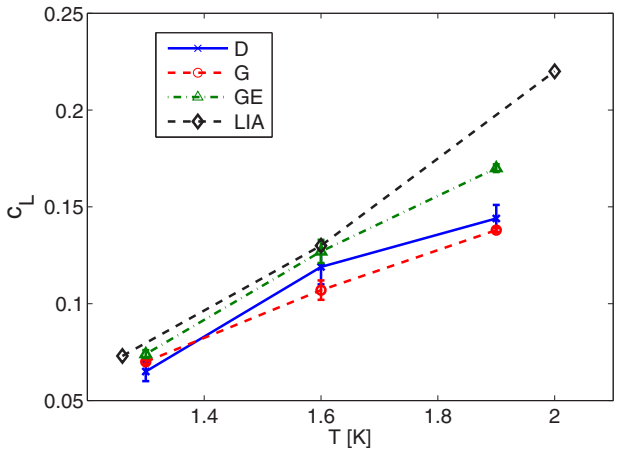

FIG. 10. (Color online) The coefficient c_L found in our VFM simulations with full Biot-Savart equations for different reconnection criteria and the LIA-VFM simulations of Schwarz [19].

within the local induction approximation $\gamma_v = \gamma_s$. However, the values of γ_s obtained with Schwarz's values of c_L are smaller than γ_v.

Comparing Eqs. (2a) and (19), we find that both Γ and $c_L/\widetilde{\Lambda}$ relate the counterflow velocity to the vortex line denisity. Therefore we can expect that the numerical smallness of $\Gamma \sim c_L \sim 0.1$ as well as their temperature dependence have similar origin. For $c_L = I_\ell/c_2^2$, it is the RMS curvature scaling coefficient c_2 that mostly defines the value and T dependence. Some discrepancy in the behavior of c_L and γ, calculated from our tangles with different reconnection criteria suggests that there is no one-to-one correspondence between these two parameters. More than one mean property of the tangle is responsible for the value of steady-state vortex line density in Biot-Savart simulations. However, for low and moderate temperatures (or low values of $\mathcal{L}$), the estimates of γ via mean tangle properties are quite accurate.

5. *Intercept velocity*

The values of v_0 found in our simulations are shown in Table III. The values are quite small, about 0.03–0.06 cm/s, but definitely nonzero within our accuracy of measurement. The values of v_0 are very different for different reconnection criteria, including some negative values for GC. Therefore we tend to consider nonzero values of v_0 not as a solid prediction of our simulations, but rather as an artefact stemming from the approximate character of the reconnection criteria. As for the larger values of $v_0^{\rm exp} \sim 0.1$ cm/s observed in experiments [17], they may be related to the strong pinning of quantized vortices on rough wall surfaces. This effect was not accounted for in our simulations. Arguments in favor of this statement may by found in Fig. 8 of Ref. [17], which shows that the experimental values of v_0 monotonically decrease for wider and wider channels. Overall, we tend to think that the finiteness of the intercept velocity v_0 is a finite size effect.

B. Mean tangle anisotropy

The counterflow velocity defines the preferred direction in the tangle. The tangle anisotropy index $I_{||}$ and the ratio $I_\perp/I_{||}$ are shown in Fig. 11. The temperature dependence [Fig. 11(a)] is consistent with the known picture [19,22] that the tangle becomes more oriented in the direction perpendicular to the counterflow velocity with increasing temperature. This may be understood as an interplay of two contributions to Eq. (10b): the term proportional to α is oriented in the plane perpendicular to V_{ns}, while the term proportional to α' is locally parallel to the counterflow velocity and leads to isotropization of the loop orientation. The ratio α'/α diminishes upon increasing the temperature and so does the relative contribution of the this term, and the tangle become more oblate.

In our simulations, the DC systematically gives the most anisotropic tangle, while GC gives the most isotropic tangle. For all simulations, $I_{||}$ is almost independent of V_{ns}, however, for both GC and GEC, a slight dependence on V_{ns} exceeding the error bars was observed [see Fig. 11(b)] for $T = 1.6$ K (not shown) and $T = 1.9$ K. This is at variance with the results of Ref. [22] where no such dependence was observed (for

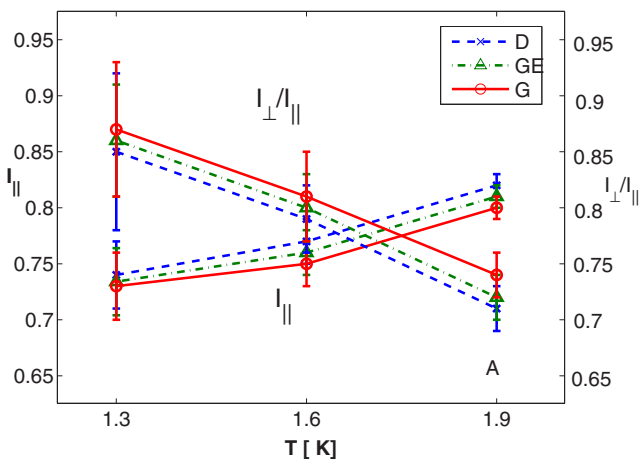

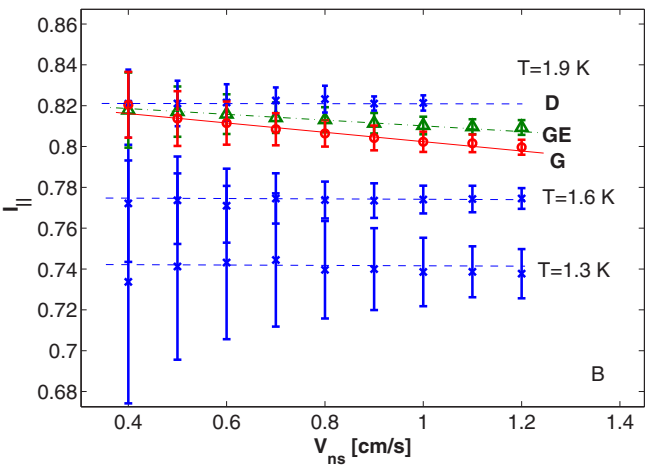

FIG. 11. (Color online) (a) The temperature dependence of the anisotropy indices $I_{||}$ and the ratio $I_\perp/I_{||}$, Eqs. (4a) and (4b). Blue crosses (×) stand for DC, green triangles (Δ) for GEC, and red circles for GC. (b) The anisotropy index $I_{||}$ vs V_{ns}. For $T = 1.3$ and 1.6 K, only D results are shown (see text). The lines serve to guide the eye.

$V_{ns} \leqslant 0.6$ cm/s), while the values of $I_{||}$ and of the ratio $I_\perp/I_{||}$ agree well with their results, as well as with the numerical results of Schwarz[19] and the experimental data by Wang *et al.* [11].

The values in Fig. 11(b) are the time averaged values and the error bars are defined by the standard deviation of $I_{||}$ for $I_{||}$ and as a sum of standard deviations of $I_{||}$ and $I_\perp$ for $I_\perp/I_{||}$ over the same time period. The values in Fig. 11(a) are the average values for a given temperature and the error bars are the largest error bars for $V_{ns} \geqslant 0.4$ cm/s.

The anisotropy indices I_ℓ and $I_{\ell\perp}$ are practically independent of V_{ns} for all temperatures and all criteria. $I_{\ell\perp}$ is close to zero in all the simulations indicating that the tangles are isotropic in the direction perpendicular to the counterflow velocity. $I_\ell \approx 0.5$ and slightly increases with temperature (see Table IV). No measurable difference for different reconnection criteria was observed.

C. Mean and RMS vortex line curvature

Next important mean characteristic of the tangle is its RMS curvature $\widetilde{S} = \sqrt{\langle |s''|^2 \rangle}$, plotted in Fig. 12(a), as a function of the $\mathcal{L}$ for different temperatures. One sees that the curvature $\widetilde{S}$ is increasing with tangle density as $\sqrt{\mathcal{L}}$ according to Eq. (5c) with the numerical prefactor c_2 that decreases as temperature grows. In other words, for the same density of the vortex lines the tangle is more curved at lower temperatures. Table IV shows that the scaling is well-obeyed in simulations with all reconnection criteria and the coefficients c_1 and c_2 are quite close. The value of c_2, calculated at $T = 1.9$ K with GC agrees well with the result of Ref. [63] ($c_2 = 1.99 \pm 0.38$).

However, some differences in the fine structure may be seen in Fig. 12(b), showing the ratio of the mean radius of curvature $R = 1/\widetilde{S}$ to the intervortex distance ℓ. In this way, we compensate the $\sqrt{\mathcal{L}}$ dependence of the curvature and the lines are almost flat. This ratio is distinctly different for different temperatures: the mean radius of curvature is about a third of the intervortex distance at $T = 1.3$ K and it grows to more than a half of ℓ for $T = 1.9$ K.

The strongest change in the structure is for DC; it has the smallest R/ℓ at $T = 1.3$ K, while for $T = 1.9$ K, it appears smoother and the ratio coincides with that for GEC. For moderate and high temperatures, the DC local structure appears the most sinuous.

The ratio R/ℓ, shown in Fig. 12(b), gives interesting *global* information about the relation between the RMS curvature and the mean intervortex distance. However, it does not allow to distinguish whether the small values of R are due to dominant contributions of small loops with large curvature, while the large loops are smooth, or because the large loops are fractal. To answer this and similar questions, we need to have more detailed information on the vortex tangle, not only its mean characteristics.

D. Drift velocity of the vortex tangle V_{vt}

In some physical problems, like the evolution of neutron-initiated micro-Big-Bang in superfluid ^{3}He-B [64], an important role is played by the drift velocity V_{vt} of the tangle with respect to the superfluid rest frame. The natural expectation is

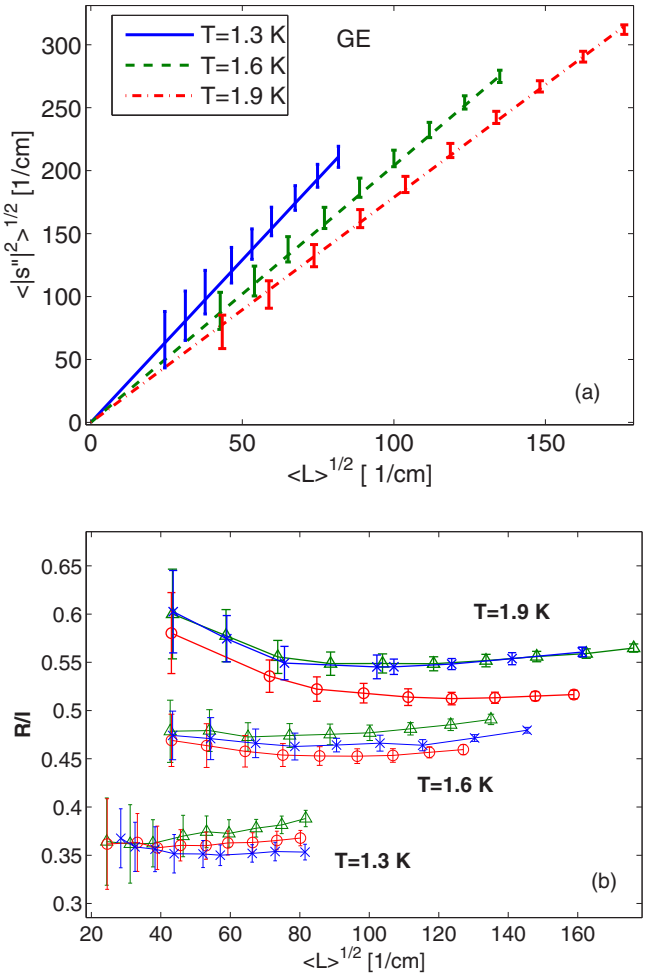

FIG. 12. (Color online) (a) The mean curvature of the tangle vs the tangle density (GEC). Symbols with error bars are data, lines are linear fit according to Eq. (5c). (b) Ratio of the mean radius of curvature to the intervortex distance. Red circles denote data for GC, green triangles for GEC, and blue crosses for DC. Lines serve to guide the eye only.

that V_{vt} is proportional to and oriented along V_{ns}. In Fig. 13(a), we plot V_{vt} calculated according to Eq. (7a). We see that the linear relation (7b) is well-obeyed. The value of V_{vt} is fully defined by its z-component, parallel to the direction of counterflow velocity, while two other components are zero within our accuracy of measurement.

As in case of c_L, the coefficient C_{vt} may be analytically related to the structural parameters of the tangle in the local induction approximation by plugging $d\boldsymbol{s}/dt$, Eq. (10b), with $\boldsymbol{V}_{si}^{LIA}$ into (7a) and by considering different contributions to the integral [19]:

$$C_{vt}^{LIA} \approx [c_L(1-\alpha')I_\ell + \alpha' I_{||}]. \tag{20}$$

The superscript "LIA" stresses the fact that this relation is not exact but obtained in the local induction approximation. The terms proportional to α are vanished in this equation by symmetry. Note that $\alpha' = O(10^{-2})$ and therefore $C_{vt}^{LIA} \approx c_L I_\ell$, which is the value plotted in Fig. 31 of Ref. [19].

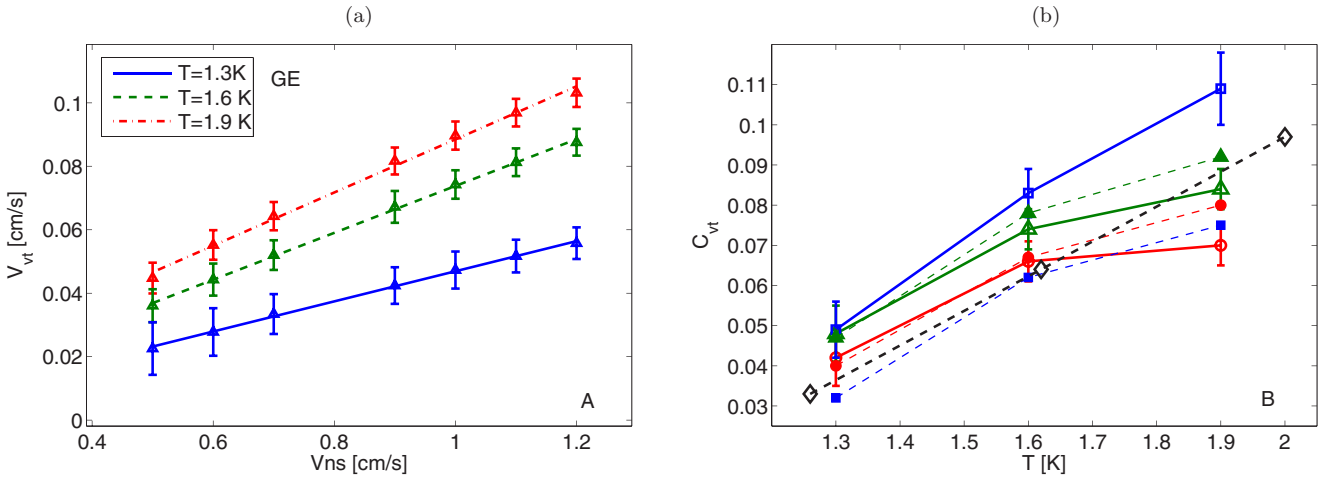

FIG. 13. (Color online) (a) Drift velocity vs V_{ns} for three temperatures. The symbols with error bars are data, the lines are the fit according to Eq. (7b). GE criterion. (b) The drift velocity coefficient C_{vt} as a function of temperature for different reconnection criteria and their LIA estimates Eq. (20). Thick solid lines with open symbols are C_{vt} obtained by fit Eq. (7b) (red cicles: GC, green triangles: GEC, blue squares: DC). Thin dashed lines with filled symbols are the LIA estimates C_{vt}^{LIA} Eq. (20) (the symbols and colors are the same as for C_{vt}). The thick dashed line with open diamonds are the results of Schwarz[19].

As we mentioned, the local contribution (11a) provides up to 90% of the total vortex velocity. Therefore we can expect that Eq. (20) will be valid with accuracy about 10%. To check this we compare in Fig. 13(b) the coefficients C_{vt}, obtained directly by fitting plots V_{vt} versus V_{ns}, presented in Fig. 13(a), and coefficients C_{vt}^{LIA}, given by Eq. (20), in the RHS of which we used mean vortex parameters, found in our full Biot-Savart simulations. First of all, we note that the drift coefficients for different criteria are close at $T = 1.3$ K but differ significantly at $T = 1.9$ K with C_{vt} for DC being almost twice larger than that for GC. Also, for DC, the coefficients increase almost linearly with temperature, while for both GEC and GC the growth slows down at $T = 1.9$ K. One sees that C_{vt} and C_{vt}^{LIA} are very close for GC and GEC, except for $T = 1.9$ K, where C_{vt} is larger. Surprisingly, C_{vt}^{LIA} for DC is *smaller* than Biot-Savart results for all temperatures, and in fact, smaller than most of the other values. The possible reason is that the drift velocity is very sensitive to the nonlocal effects on the local tangle structure for more dense tangles (DC always gives denser tangles).

The Schwarz's C_{vt}^{LIA} found from Eq. (20) in the RHS of which the mean vortex parameters are found by simulations in the LIA [19] is very close to the GC results (both C_{vt} and C_{vt}^{LIA}) for $T = 1.3$ and 1.6 K, but is somewhat larger than C_{vt}^{LIA} for $T = 1.9$ K. Comparing with Fig. 10, we see that the difference in the tangle structure (I_ℓ in this case) between Biot-Savart and LIA simulations is important: for c_L, the GEC results were closer to Schwarz's values. Therefore the particular closeness of different Schwarz's results to our results with different reconnection criteria is not systematic and should be taken with caution.

The main and well-expected physical message is that C_{vt} is small (below upper limit of $V_{vt}/V_{ns} = 0.2$, suggested in Ref. [65] and in accord with results of Ref. [11]). This means that the tangle velocity is close to the superfluid velocity and its slippage is about 5% at $T = 1.3$ K and close to 10% at $T = 1.9$ K.

E. Mutual friction force F_{ns}

The scaling of the mutual friction force $F_{ns} \propto V_{ns}^3$ is well-obeyed in all simulations with all three criteria, as we illustrate in Fig. 14(a) for GE criterion. Their fit allows to find coefficients C_f plotted in Fig. 14(b).

Notice that an analytical expression for C_f can be found by considering different contributions to the integral J in Eq. (8a) with the only local-induction contribution to the vortex velocity V_{si}^{LIA} [19]:

$$C_f^{LIA} \approx \left(\frac{c_L}{\widetilde{\Lambda}}\right)^{2/3} (I_\parallel - c_L I_\ell)^{1/3}. \qquad (21)$$

Like in Eq. (20), we have added here superscript "LIA" to stress the approximated character of the relation obtained in the local induction approximation.

In Fig. 14(b), we compared the coefficients C_f and C_f^{LIA} for different reconnection criteria. One sees that they almost coincide for $T = 1.3$ K. At $T = 1.9$ K, our results show significant spread of about 25% with $C_f = 0.22$ for GC and 0.29 for DC. There is again a discrepancy in the behavior of C_f^{LIA}; while for GC and GEC, $C_f^{LIA} > C_f$, especially for $T = 1.9$ K, the LIA estimate is smaller than C_f for DC at all temperatures. The results of Schwarz[19] are larger than our values of C_f and their LIA estimates. Interestingly, here the results for DC are the closest to Schwarz's results, including linear in T behavior, albeit the largest VLD and, therefore, worst conditions for comparison with LIA results. This again confirms that the closeness of LIA and Biot-Savart results should not be taken too seriously.

The coefficient C_f is directly related by Eq. (8d) to the more experimentally used Gorter-Mellink constant A_{GM}. We plot in Fig. 15 the values of A_{GM} obtained as a fit according to Eq. (8c) as well as some experimental data. The experimentally measured values of A_{GM}, summarized by Arp [66], show significant spread. We only plot the results of Vinen [9] and Kramers *et al.* [67] (as cited by Arp [66]). As it is clearly seen, all our values (except for GC at $T = 1.9$ K) fall between the

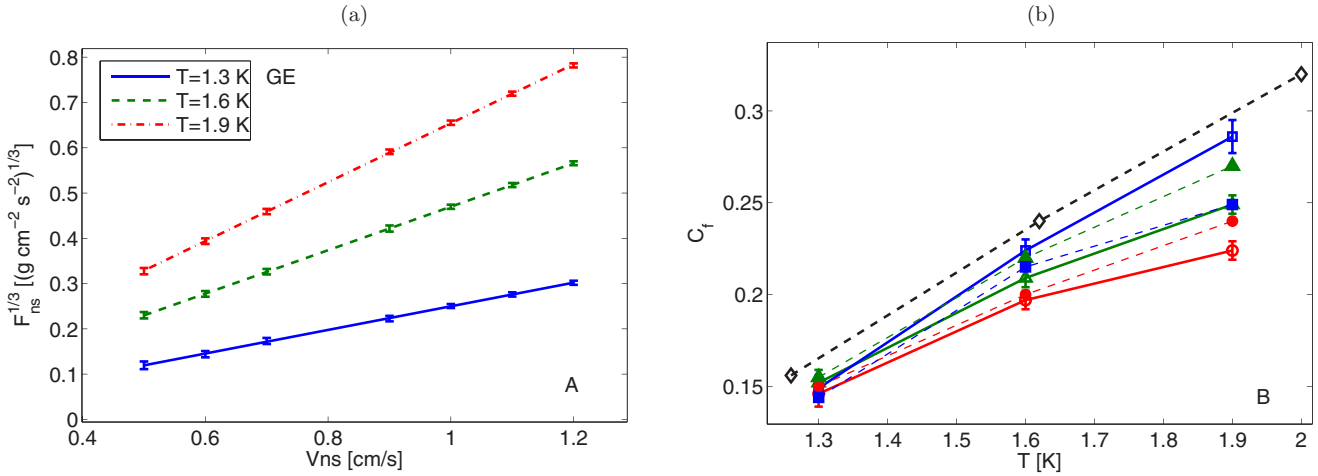

FIG. 14. (Color online) (a) The friction force density (8a) vs counterflow velocity V_{ns}. The symbols with error bars are data, the lines are fit according to Eq. (8b), GE criterion. (b) The friction force coefficients C_f as a function of temperature for different reconnection criteria and their LIA estimates. Thick solid lines with open symbols are C_f obtained by a fit according to Eq. (8b) (red cicles GC, green triangles GEC, blue squares DC). Thin dashed lines with filled symbols are the LIA estimates C_f^{LIA}, see Eq. (21) (the symbols and colors are the same as for C_f). The thick dashed line with open diamonds are the results of Schwarz [19].

representative experimental results. This means that (i) we get the correct order of magnitude and correct T dependence of the Gorter-Mellink coefficient [68], and (ii) the direct comparison with particular experimental results is complicated and subject to the same difficulties as for γ.

F. Mean and most probable loop lengths

The temperature and V_{ns} dependence of the mean loop length $\overline{L}$ are shown in Fig. 16. One sees that at $T = 1.3$ K, $\overline{L} \approx 0.33$ cm for both $V_{ns} = 0.5$ and 1 cm/s but their T dependence is different: $\overline{L}$ *increases* with T for $V_{ns} = 0.5$ cm/s and *decreases* for $V_{ns} = 1$ cm/s. Remarkably, the most probable loop length defined in Eq. (22) and also shown in Fig. 16, is essentially smaller, falling below 0.015 cm for the most dense tangle ($T = 1.9$ K and $V_{ns} = 1$ cm/s). We return to this fact below in Sec. VI A.

VI. DETAILED STATISTICS OF THE VORTEX TANGLE

As we mentioned in Introduction, the mean characteristics of the vortex tangle, studied in the previous section, Sec. V, provide important but very limited information on the tangle properties. Much more detailed statistical information on local tangle properties is required for a better understanding of basic physics of counterflow turbulence as well as for further advance in its analytical studies. This information may be obtained from probability distribution functions of local tangle properties (like line curvature), of global vortex-loop characteristics (e.g., their lengths) and from corresponding

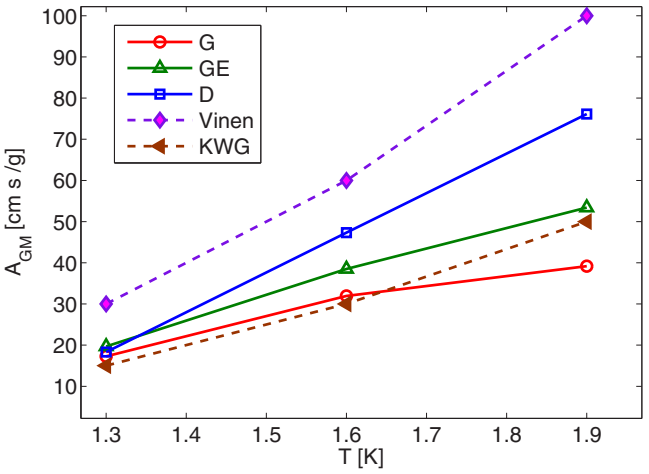

FIG. 15. (Color online) The Gorter-Mellink coefficients A_{GM} as a function of temperature for different reconnection criteria. Solid lines with open symbols are A_{GM} obtained by fit according to Eq. (8c). The dashed lines with filled symbols are the experimental results of Vinen [9] and Kramers, Wiarda, and van Groenou [67].

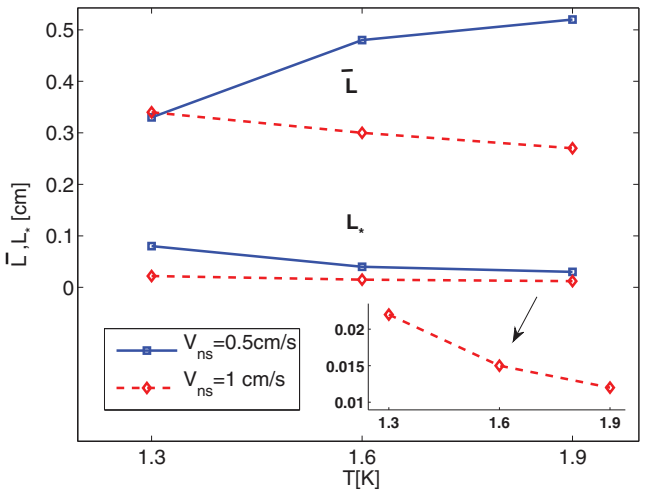

FIG. 16. (Color online) Comparison of the mean loop length $\overline{L} \sim (0.3 \div 0.5)$ cm and the most probable loop length $L_* \sim (0.08 \div 0.01)$ cm at different temperatures and values of V_{ns}. Inset shows details of L_* for $V_{ns} = 1$ cm/s. GEC.

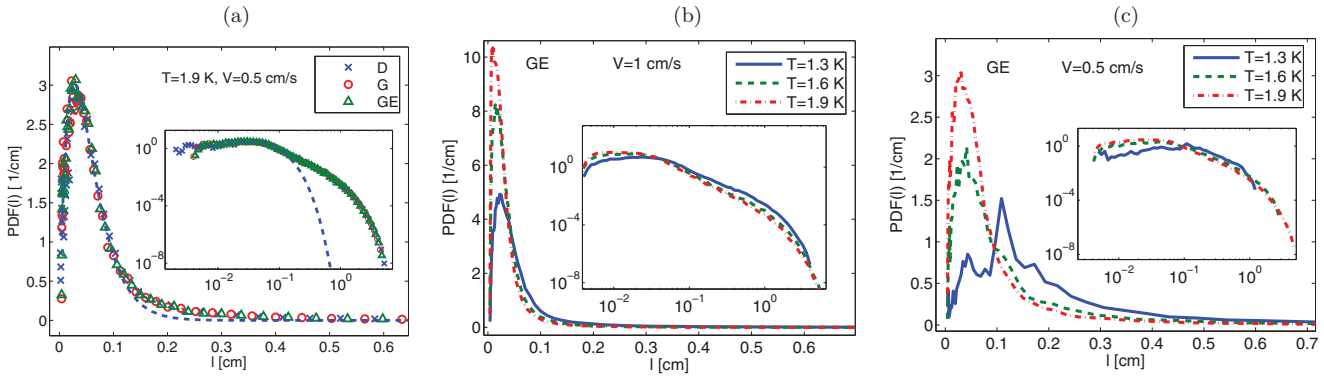

FIG. 17. (Color online) PDF of the vortex-loop length l, $\mathcal{P}(l)$. (a) $T = 1.9$ K, $V_{ns} = 1$ cm/s, three reconnection criteria. Blue dashed line shows exponential core of the PDF (22). (b) $V_{ns} = 1$ cm/s, for $T = 1.3$, 1.6, 1.9 K, GEC. (c) $V_{ns} = 0.5$ cm/s, for $T = 1.3$, 1.6, 1.9 K, GEC. Insets show the same PDFs in log-log scale.

(cross)-correlation functions (e.g., of vortex line orientations, of loop length versus mean curvature). Bearing in mind that this information will not be available from experiments in foreseeable future, the only way to get it today is from numerical simulations. This is the motivation and the subject of the present section.

The probability distribution functions discussed in this section were calculated over all the steady-state tangle configurations, computed for a particular T and V_{ns}.

A. Probability density function (PDF) of vortex-loop lengths

Turning to a more detailed description of the tangle structure we plot in Fig. 17 the PDF of the vortex-loop length, $\mathcal{P}(l)$ for $T = 1.3$, 1.6, 1.9 K and $V_{ns} = 0.5$, 1.0 cm/s. Panel (a) shows that $\mathcal{P}(l)$ is practically independent of the reconnection criterion at least for cases with moderate to large line density.

The second observation is that the core of the PDF $\mathcal{P}(l)$ may be approximated by a simple formula:

$$\mathcal{P}(l) \simeq \psi \mathcal{P}_0(l), \quad \mathcal{P}_0(l) \equiv \frac{l}{L_*^2} \exp\left(-\frac{l}{L_*}\right), \qquad (22)$$

shown in Fig. 17(a), left, by the blue dashed line. The function $\mathcal{P}_0(l)$ is normalized to unity: $\int_0^\infty \mathcal{P}_0(l)\, dl = 1$. The fitting parameter L_* corresponds to the maximum of the core function (22) and simultaneously to the maximum of $\mathcal{P}(l)$. Therefore we called it the most probable length as plotted in Fig. 16. The second fitting parameter ψ shows the fraction of loops that belong to the core and define L_*. The value of $\psi \simeq 0.2$ for $V_{ns} = 0.5$ cm/s and $\psi \simeq 0.3$ for $V_{ns} = 1$ cm/s is only very weakly dependent on T. We conclude that the majority of loops belongs to the long tail, which is clearly seen in the insets in Fig. 17. For loop lengths slightly exceeding 0.1 cm, the PDF tails exhibit a power-law-like behavior over an interval of lengths about half a decade with a nonuniversal exponent ranging between -2 and -3 for different V_{ns} and temperatures. The mean value of the loop length $\overline{L}$ is determined by the tails and, as we have shown in Fig. 16, is much larger than L_*.

Panels (b) and (c) of Figs. 17 show how $\mathcal{P}(l)$ varies with temperature and V_{ns}. As we know, with increasing T and V_{ns} the VLD increases, the intervortex distance becomes smaller and the reconnection rate increases. All that shifts the PDF $\mathcal{P}(l)$ toward shorter loops. For the least dense case ($T = 1.3$ K and $V_{ns} = 0.5$ cm/s), the PDF looks very indented, probably because of the lack of statistics.

B. PDF of the line curvature

The next object of interest is the PDF of local curvatures $\mathcal{P}(|s''|)$, shown in Fig. 18 for $T = 1.3$, 1.6, 1.9 K and $V_{ns} = 1$ cm/s. These PDFs linearly vanish for $|s''| < \widetilde{S}$ and exponentially vanish for $|s''| > \widetilde{S}$. We suggest an interpolation formula between these two asymptotes, which is very similar to Eq. (22):

$$\mathcal{P}(|s''|) \simeq \frac{6\,|s''|}{\widetilde{S}^2} \exp\left(-\frac{\sqrt{6}\,|s''|}{\widetilde{S}}\right). \qquad (23)$$

Notice that Eq. (23) has no fitting parameters, it just involves the RMS curvature $\widetilde{S}$. As one sees in an inset in Fig. 18, this equation describes reasonably well the entire form of $\mathcal{P}(|s''|)$. Accepting Eq. (23), we can find the ratio $\overline{S}/\widetilde{S} = \sqrt{2/3}$. Correspondingly, the ratio c_1/c_2 defined by Eq. (5c) is also $\sqrt{2/3}$. This prediction agrees well with our numerical results

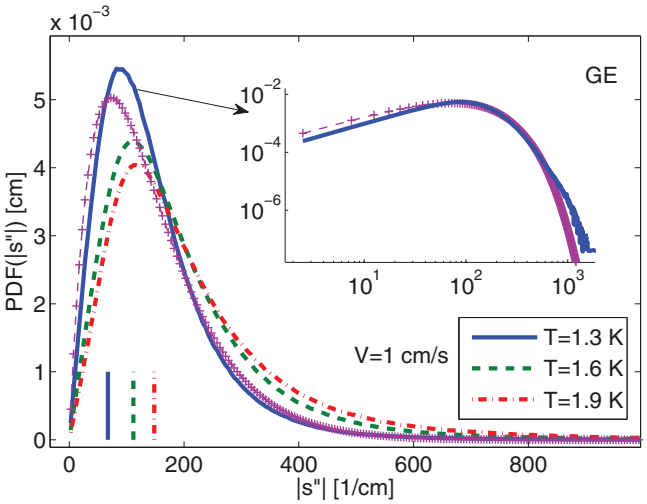

FIG. 18. (Color online) PDF of local line curvature for three temperatures and $V_{ns} = 1$ cm/s, GEC. Vertical lines near the horizontal axis show $1/\ell$ at given conditions. (Inset) PDF(s) for $T = 1.3$ K (blue solid line) and the fit by Eq. (23) (purple crosses).

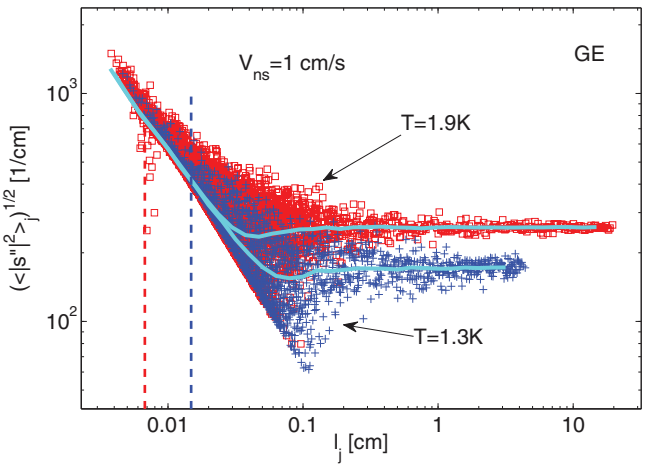

FIG. 19. (Color online) Diagrams of RMS of loop-curvature $\widetilde{s}''_j$ vs loop-length l_j for $V_{\rm ns} = 1$ cm/s with GEC for two temperatures. The plus sign(+) denote data for $T = 1.3$ K, the squares are for $T = 1.9$ K. Light blue lines correspond to the mean curvature of loops vs their length. The intervortex distances are denoted by vertical dashed lines: for $T = 1.9$ (left) and 1.3 K (right).

for c_1 and c_2 given in Table IV. For example, for GEC, the ratio $\sqrt{3}c_1/\sqrt{2}c_2$ is equal to 0.985, 1.009, and 1.018 (instead of the predicted value of unity) for $T = 1.3$, 1.6, and 1.9 K, respectively.

This equation also allows us to find the most probable curvature $S_* \simeq \widetilde{S}/\sqrt{6} \simeq \overline{S}/2$. All three characteristic curvatures are determined by the exponential PDF (23) and therefore they are of the same order of magnitude. This is different from the characteristic loop lengths, where L_* is determined by the exponential core of the PDF (22), while $\overline{L} \gg L_*$ is determined by the long power-law tail of the PDF.

C. Correlation between loop length l_j and RMS of the loop curvature $\widetilde{s}''_j$

Knowing the PDFs (22) and (23), of the loop length and line curvature separately we now come to the next question: how are these objects correlated? In particular, do all loops (long and short) have more or less the same RMS and mean curvatures $\widetilde{s}''_j$ and $\overline{s''_j}$ [defined by Eq. (6)] or do short loops have larger values of $\widetilde{s}''_j$? To resolve this question, we plot numerous $(\widetilde{s}''_j, l_j)$ points belonging to all loops in the statistical set of the tangle configurations, computed for particular T and $V_{\rm ns}$. These points form a $(\widetilde{s}''_j - l_j)$ diagram shown in Fig. 19 for $T = 1.3$ and 1.9 K with $V_{\rm ns} = 1$ cm/s.

The majority of points are located to the left of $l_j = 0.1$ cm according to the PDFs $\mathcal{P}(l_j)$ shown in Fig. 17. Next, for small l_j below 0.1 cm, one sees a sharp boundary that restricts from below the available S_j at given l_j. This boundary corresponds to the minimal possible RMS loop curvature $\widetilde{s}''_j = 2\pi/l_j$, realized for an ideal circle of radius $1/\widetilde{s}''_j$ with $l_j = 2\pi/\widetilde{s}''_j$. Some points below this line for small l_j are the result of the finite space resolution in the continuous vortex line presentation via a discreet set of points: the smallest loops, displayed in Fig. 19 are parameterized by only three points. Long loops have curvatures well-concentrated around the conditional (with fixed l) RMS value

$$\widetilde{S}(l) = \langle \widetilde{s}''_j \rangle_{l_j = l}, \tag{24}$$

shown in Fig. 19 by blue lines (upper line for $T = 1.9$ K and by the lower line for $T = 1.3$ K). One sees that $\widetilde{S}(l)$ is practically independent of l for l that exceeds substantially the intervortex distance ℓ, denoted by vertical lines. This is an evidence in favor of the natural expectation that local properties of long loops are independent of their total length.

D. PDFs of the mean and RMS loop curvature

Full information about the statistical distribution of $\widetilde{s}''_j$ for loops with given length l can be found from the conditional PDF, $\mathcal{P}(\widetilde{s}''_j, l_j = l)$. In particular, this PDF would describe the difference in properties of short and long loops. Nevertheless, in the beginning, we will restrict ourselves to an analysis of less detailed information: the unconditional PDFs of the mean and the RMS loop curvature, $\mathcal{P}(\overline{s''})$ and $\mathcal{P}(\widetilde{s}'')$, shown in Figs. 20(a), 20(b), 20(d), and 20(e). In panels (a) and (d), we compare these PDFs for the three reconnection criteria with $T = 1.3$ K and $V_{\rm ns} = 1$ cm/s. They look similar, at least on a semiquantitative level. Therefore, to clarify how these PDFs vary with T and $V_{\rm ns}$, it would be sufficient to analyze the results for GEC only, as shown in panels (d) and (e). One sees that these PDFs agree with the fact that the mean and RMS curvatures of the tangle increase with density (or $V_{\rm ns}$) for a given temperature and are smaller for higher temperatures for the same density (Fig. 12, top).

Both PDFs, $\mathcal{P}(\overline{s''})$ and $\mathcal{P}(s'')$, may be roughly approximated as a narrow peak of some width σ, which is much smaller than the position of its maximum. PDF of the mean curvature looks more regular. Its core is approximated well enough by a Gaussian,

$$\mathcal{P}(\overline{s''}) \approx \frac{\psi}{\sqrt{2\pi}\sigma} \exp\left[-\frac{(\overline{s''} - \overline{s''_*})^2}{2\sigma^2}\right], \tag{25}$$

with three fitting parameters: the position of the maximum $\overline{s''_*}$ (the most probable mean-loop curvature), the width σ, and the total amount ψ of $\overline{s''}$, described by the core of PDF (25): $\int \mathcal{P}(\overline{s''}) d\overline{s''} = \psi$. This allows us to quantify the differences between curvature distributions in a wider range of parameters. The temperature dependencies of $\overline{s''_*}$, σ, and ψ are shown in Figs. 20(c) and 20(f) for $V_{\rm ns} = 0.5$ and 1.0 cm/s, respectively. One sees that ψ is quite close to unity: $\psi > 0.9$ at $V_{\rm ns} = 0.5$ cm/s and $\psi > 0.8$ at $V_{\rm ns} = 1$ cm/s for all three reconnection criteria. This means that Eq. (25) describes reasonably well the entire PDF and not only its core. Therefore, at our level of description, the contribution of nonexponential tail can be ignored.

Notice that on a semiquantitative level there are no differences in the values and behaviors of $\overline{s''_*}$ and σ for the three reconnection criteria. Therefore in Figs. 20(c) and 20(f), we presented these parameters only for GEC. In addition, we show (by blue dashed lines) in the same panels the overall (over the entire tangle) mean value of the curvature $\overline{S}$, which, by definition, has to coincide with the mean (over different loops) of the mean-loop curvature: $\overline{S} = \int \overline{s''} \mathcal{P}(\overline{s''}) d\overline{s''}$. We see that the mean

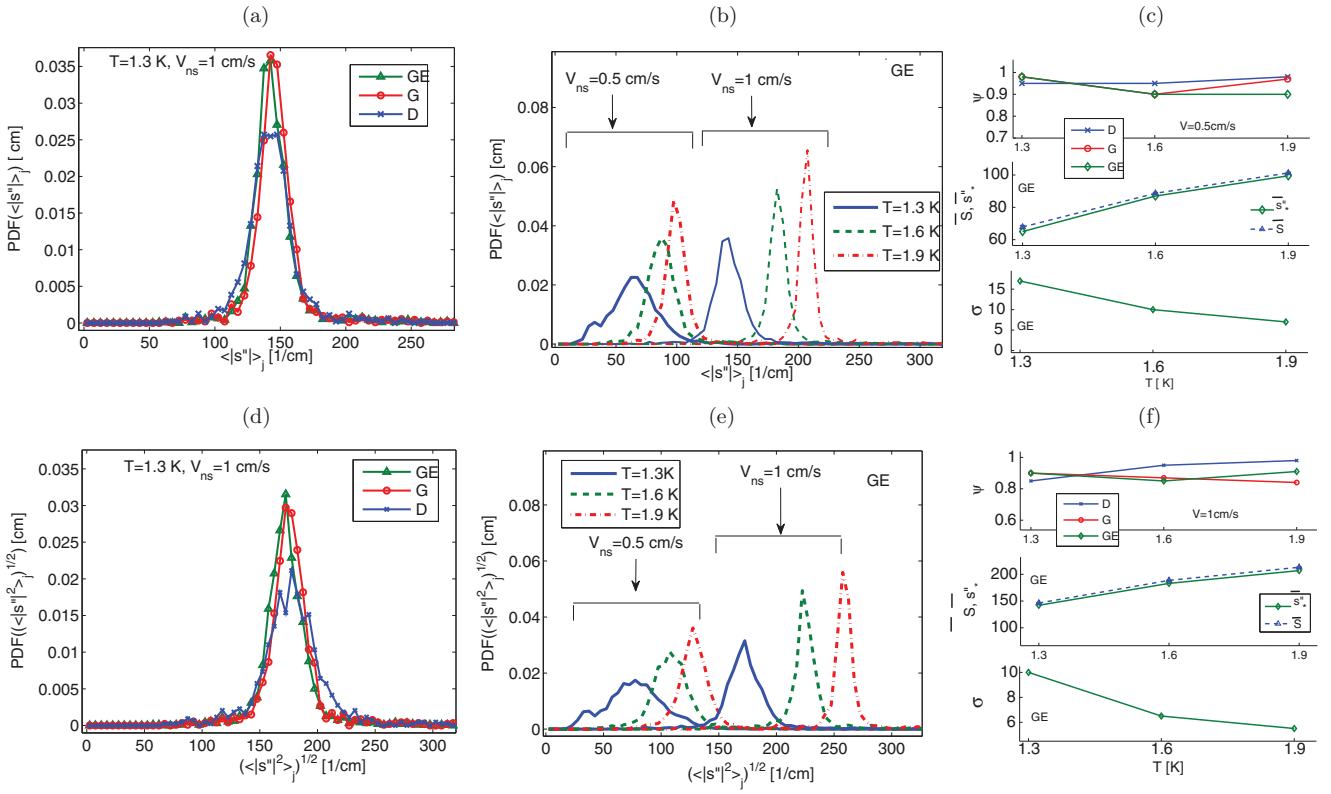

FIG. 20. (Color online) Comparison of PDFs of the mean (a) and RMS (d) loop curvature for three reconnection criteria ($T = 1.3$ K and $V_{ns} = 1$ cm/s). The lines serve to guide the eye only. Temperature and V_{ns} dependence of the PDF of the mean (b) and RMS (e) loop curvature (for GEC). Parameters of the Gaussian fit (25) for the PDF of the mean curvature are shown in (c) for ($V_{ns} = 0.5$ cm/s) and (f) for ($V_{ns} = 1$ cm/s).

tangle curvature $\overline{S}$ practically coincides with the most probable mean-loop value $\overline{s''_*}$. This means that the role of the PDF tail can be ignored, as we stated above on the basis that $\psi \simeq 1$.

The next observation is that $\overline{s''_*}$ (and $\overline{S}$) increases with temperature and counterflow velocity, i.e., with the tangle density. This agrees with the well-known fact of $\overline{S} \propto \sqrt{\mathcal{L}}$. A less expected observation is that σ decreases with increasing T and V_{ns}, i.e., in the denser tangle, the mean-loop curvatures are less spread around their mean (or most probable) value.

E. Autocorrelation of the vortex orientation

It was recognized by Schwarz [58] that the structure of the vortex lines is reminiscent of random walks. As the vortex segments get further apart, their relative orientation becomes more random. To find out at which distances the correlation between the segment orientation is lost, we plot in Figs. 21(a) and 21(b), the orientation correlation function $K(\boldsymbol{r}_1 - \boldsymbol{r}_2)$, defined by Eq. (9).

A crucial observation is that the correlation falls off very fast being almost zero at the intervortex distance. This result supports Nemorivskii's Gaussian model of ^{4}He-vortex tangle [69], in which correlation of the orientations disappears at intervortex distance ℓ and the mean loop length $\overline{L} \gg \ell$.

Interestingly, for weak counterflow velocities $V_{ns} = 0.5$ cm/s, there is a distinct negative correlation (the segments are antiparallel) at distances just beyond ℓ. This can be related with the tendency of close vortex lines to become antiparallel on the way to reconnection. For stronger $V_{ns} = 1$ cm/s, i.e., in more dense tangles, this tendency is masked by the influence of other neighboring vortex lines. Therefore such an antiparallel orientation is not observed.

Averaging these correlation functions over all distances, we find that on average the tangle is slightly polarized and this polarization K depends on the intervortex distance ℓ, but not on the temperature: see Fig. 21(c) where we plot K as a function of ℓ for three temperatures. The value of ℓ at given T was varied by the counterflow velocity. Here again, there is no noticeable difference in the values and dependencies of $K(\boldsymbol{r}_1 - \boldsymbol{r}_2)$ and K for different reconnection criteria, therefore only GEC case is displayed.

The most important observation in Fig. 21(c) is that $\overline{K} \sim 10^{-3}$, i.e., it is vanishingly small with respect to unity. This means that there is no coherent contribution (of many vortex lines) to the velocity field at large scales (much above ℓ). Therefore the energy spectrum of the turbulent vortex tangle, $E(k)$, has to be determined by contributions of individual vortex lines even for $k\ell \ll 1$, up to the box size.

VII. ON THE PHYSICS OF ^{4}He COUNTERFLOW TURBULENCE

In this section, we present a summary of the results obtained here and in other studies of counterflow turbulence.

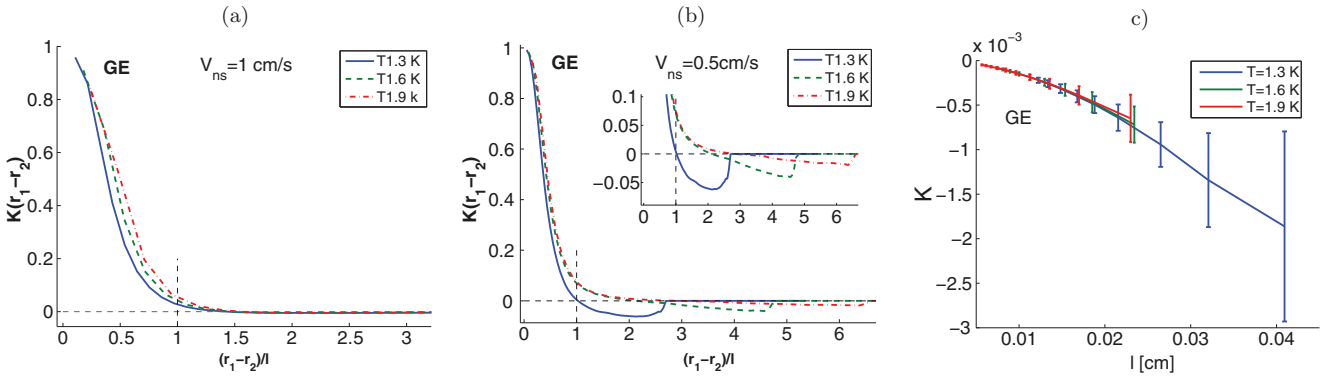

FIG. 21. (Color online) (a) and (b) The orientation correlation function for different temperatures and two counterflow velocities. (Inset) details of long distance tail. The distance is measured in units of intervortex distance. (c) The mean polarization of the tangle as a function of the intervortex distance. GEC.

A. Idealizations and relevant parameters

1. Spatial homogeneity

In analogy to classical hydrodynamic turbulence, the basic models of counterflow turbulence are based on the assumption of spatial homogeneity of the problem. In laboratory experiments on counterflow in ^{4}He, this can be realized to some extent in a wide channel or a pipe of transverse size H that significantly exceeds the intervortex distance ℓ. For example, in the superflow experiments of Ref. [17], the largest $H = 1$ cm, while ℓ varies (approximately) from 0.1 to 4×10^{-4}cm (for $V_{\rm ns} \simeq 20$ cm/s).

In numerical simulations (like ours), the homogeneity can be simply reached with periodic boundary conditions. Again, the size of the box H (cube in our case) should be larger than ℓ. In our simulations, $H = 0.1$ cm, while ℓ varies from 0.005 cm to 0.04 , as seen in Fig. 5.

One additional simplifying assumption made in our study (and many others) is that the flow of the normal component is laminar. In numerical simulations (including ours), this simply requires $V_{\rm n} = $ const. In experiments, this is achieved to some extent in a core of a wide-channel counterflow, when $V_{\rm ns}$ is below some critical value $V_{\rm cr}$, above which the normal fluid flow is expected to become turbulent. Probably a better realization of the laminarity assumption in laboratory experiments is achieved in the "pure" superflow, where normal fluid flow is prevented by superleaks, a kind of (e.g., silver) porous medium with submicrometer size pores to prevent a net flow of the viscous normal component through the channel on any experimentally relevant flow time scale, see, e.g., Ref. [17]. Now, if one neglects the $V_{\rm n}$ dependence on the (transverse) distance to the wall, the entire problem can be approximated as spatially homogeneous.

In order to relax the assumption of space homogeneity, one has to develop a theory (or a model) of superfluid wall-bounded flow, which will find and account for an actual laminar super- and normal-fluid velocity profiles across a channel. This is still an open problem. Even more sophisticated and challenging open problem is a superfluid wall-bounded turbulence at large counterflow velocities, when both the normal and the superfluid components are turbulent and their mean-velocity and turbulent-energy profiles have to be found self-consistently, accounting for the mutual friction between the components. Detailed information about the vortex tangle structure, found and analyzed in this paper, is required to successfully approach this problem. This was one of the important motivations for the present study.

2. No isotropy, just axial symmetry

It is generally accepted that the classical hydrodynamic turbulence is almost isotropic at small scales $l \ll H$ due to the isotropization effect that is observed going from the outer scale H toward the small scales l. The theory of small scale turbulence then simplifies. In the counterflow case, there is no energy cascade and the superfluid counterfow turbulence is inherently anisotropic due to the builtin direction of the counterflow velocity $\boldsymbol{V}_{\rm ns}$. This anisotropy is of principal importance and cannot be ignored at all. Indeed, in the isotropic case, there is no friction force between the normal and superfluid components and the counterflow does not create a vortex tangle. One can formally see this from the following argument: consider the parameter $C_{\rm f}$ that quantifies the mutual friction and γ that determines the vortex tangle density (Secs. VA4 and VE). Both are proportional to the anisotropy parameter I_ℓ, which is equal to zero in the isotropic tangle.

Nevertheless, in a spatially homogeneous case, with the only relevant direction $\boldsymbol{V}_{\rm ns}$, one expects to see axial symmetry around $\boldsymbol{V}_{\rm ns}$. Indeed, in our simulations, the coefficient $I_{\ell\perp}$ [defined by Eq. (4d)], which is responsible for the axial asymmetry, is close to zero.

3. The physical parameters of the problem

(1) The main parameter in the problem of quantum turbulence is the circulation quantum $\kappa \approx 10^{-3}$ cm/s^{-2}.

(2) The second parameter is the vortex core radius a_0. In ^{4}He, $a_0 \simeq 10^{-8}$ cm. In the theory of counterflow turbulence, a_0 appears in combination with the intervortex distance ℓ as a dimensionless parameter $\Lambda \simeq \ln(\ell/a_0)$. More accurate definition of Λ is given by Eq. (11), where we also introduced $\widetilde{\Lambda} = \Lambda/(4\pi)$. The parameter $\widetilde{\Lambda}$ naturally appears in the equations of motion for the vortex line in the local induction approximation. Table I shows that in actual experimental situations $\widetilde{\Lambda}$ is very close to unity.

(3) Additional dimensionless parameters are α and α', which determine the mutual friction force [according to Eq. (10b)]. Of the two α is more important, being responsible for the dissipative part. As one sees in Table I, α varies in the relevant temperature range by a factor of 8, being much smaller than unity ($\alpha = 0.036$) at $T = 1.3$ and approaching unity, when T is close to T_λ, see Table I.

(4) We have also to mention the ratio of normal and superfluid densities ρ_s/ρ_n. Having in mind that the total ^{4}He density $\rho \equiv \rho_s + \rho_n$ in the problem at hands can be considered as temperature independent, we can use the ratio ρ_n/ρ instead of ρ_s/ρ_n. It varies about ten times (from 0.045 to 0.42, see Table I) in the studied temperature range.

Having so many dimensionless parameters that essentially deviate from unity and vary significantly with temperature, one may think that dimensional reasonings are useless in our problem. However, as we have shown in the paper, they are still useful. Being supplemented with simple physical arguments they give quite reasonable results, for example, to determine the V_{ns} dependence of the basic tangle characteristics, see below.

B. V_{ns} dependence of the vortex-tangle characteristics

Using dimensional reasoning with only parameter κ we reproduced a set of relationships that determined the V_{ns} dependence of the main characteristics of the vortex tangle. For concreteness, we list them in the order of increasing powers of V_{ns} and remind the values of corresponding dimensionless parameters:

(1) the mean and RMS vortex line curvature, $\overline{S} = c_1/\ell \propto V_{ns}^{-1}$, $\widetilde{S} = c_2/\ell \propto V_{ns}^{-1}$, see Eqs. (5), Fig. 12, and Table IV; $c_2 \approx \sqrt{3/2}\, c_1 \simeq 2 \div 3$.

(2) The anisotropy indices $I_\parallel$, $I_\perp$, I_ℓ, and $I_{\ell\perp}$ are practically independent of V_{ns}, i.e., $\propto V_{ns}^0$, see Eqs. (4), Fig. 11, and Table IV; $I_\parallel$, $I_\perp \simeq 0.7 \div 0.9$, $I_\ell \simeq 0.5$, $I_{\ell\perp} \approx 0$ (because of the axial symmetry).

(3) The drift velocity $V_{vt} = C_{vt} V_{ns}$, see Eq. (7b), Fig. 13; $C_{vt} \simeq 0.05 \div 0.08$.

Vortex line density $\mathcal{L} = \kappa^2 (\Gamma V_{ns})^2$, see Eq. (2a), Fig. 8, and Table III; $\Gamma \simeq 0.07 \div 0.16$.

(4) The mutual friction force density, $F_{ns} = \alpha\, \rho_s\, \kappa^{-1} (C_f V_{ns})^3$, see Eq. (8b), Fig. 14. The derivation of Eq. (8b) was based not only on dimensions of F_{ns} but also on its explicit expression (8a) via configuration of the vortex tangle, $C_f \simeq 0.15 \div 0.25$. (5) The reconnection rate $dN_r/dt = c_r \kappa \mathcal{L}^{5/2} \propto V_{ns}^5$, see Eqs. (3) and (2a), Fig. 7, and Table II; $c_r \simeq 0.4 \div 0.6$.

As one sees in the figures mentioned above, the results of our numerical simulations agree well with all these expected V_{ns} dependencies. Notice that the numerical values of the corresponding dimensionless parameters (presented above) are not always of the order of unity but often smaller by an order of magnitude. Some understanding of the reason for that can be obtained with the explicit form of the bridge relations of Schwartz's obtained using the local interaction approximation as discussed next.

C. Schwartz's bridge relations

Using the equation of motion (11) in the local interaction approximation, Schwartz [19] analytically derived the bridge relations that connect some of the parameters mentioned above. In our dimensionless notations, these are (1) $\Gamma_s \equiv \kappa \gamma_s \approx \dfrac{I_\ell}{\widetilde{\Lambda} c_2^2}$ [by comparing Eqs. (2a) and (19)]; (2) Eq. (20) for C_{vt}^{LIA}, which quantifies the tangle drift velocity V_{vt} [see Eq. (7b)]; and (3) Eq. (21) for C_f^{LIA}, which quantifies the mutual friction force density F_{ns} [see Eq. (8b)]. These equations bridge Γ_s, C_{vt}^{LIA}, and C_f^{LIA} with the tangle anisotropy parameters $I_\parallel$, I_ℓ, defined by Eq. (4) and tangle RMS curvature parameter c_2, defined by Eq. (5).

These bridge relations are fulfilled with reasonable accuracy in our simulations (with the full Biot-Savart equation), especially for low temperatures. For higher temperatures, the discrepancy increases, but overall the order of magnitude of these coefficients is close to those calculated by Schwarz (with $I_\parallel$, I_ℓ, and c_2 obtained by LIA simulations) and agree with available experimental data. This allows us to believe that the LIA may be successfully used in analytical studies of counterflow turbulence in spite of the fact that it fails in numerical simulations.

D. Probability distribution and correlation functions in the vortex tangle

Many of the mean parameters discussed above can be measured experimentally, at least in principle. However, detailed statistical information of the random vortex tangle statistics is hardly expected in foreseeable experiments. Because of their importance for better understanding the basic physics of counterflow turbulence, we put some efforts to clarify it numerically. In particular, we studied:

(1) the PDF of the vortex-loop length $\mathcal{P}(l)$ and showed that its core (which contains about $20 \div 30\%$ of the total loops) can be described by a simple exponential form (22) as seen in Fig. 17(a). It has a peak at some $L_* \sim 0.01 \div 0.02$ cm, which is much smaller than the mean loop length $\overline{L} \sim 0.3 \div 0.5$ cm, defined by the tail of the PDF, see Fig. 16.

(2) The correlation between the length l_j and the RMS curvature $\widetilde{s''}_j$ of loops with a given l_j is demonstrated in Fig. 19. We show that for long loops, $\widetilde{s''}_j$ is practically independent of their length and close to the overall RMS curvature $\widetilde{S}$, while for short loops its bounded from below by (and concentrated close to) the curvature of a circle with a given length.

(3) The PDF of the line curvature $\mathcal{P}(|s''|)$. We show that $\mathcal{P}(|s''|)$ may be well-described by an exponential form, see Eq. (23), without fitting parameters, just involving the RMS curvature $\widetilde{S}$. This allowed us to find the ratio between the structural parameters $c_1/c_2 \approx \sqrt{2/3}$.

(4) The PDFs of the mean and the RMS loop curvature. We show that more that 90% of the PDF are close to a Gaussian form (25) and studied in Sec. VI D the temperature dependence of their maxima and widths.

(5) Last but not least, the characteristics of the vortex tangle in the form of the autocorrelation function of the vortex orientation $K(\boldsymbol{r})$, defined by Eq. (9). Figure 21 shows that $K(\boldsymbol{r})$ practically vanishes at distances about ℓ. This means that vortex lines are reminiscent of a random walk with a correlation length of the order of the intervortex distance. This fact has many

important consequences, e.g., for the energy spectra in counterflow turbulence.

E. Dynamical and statistical characteristics versus reconnection criteria

We carried out full Biot-Savart simulations of the evolution of the vortex tangle within the vortex filament method in a wide range of parameters. We compared the statistical and geometrical properties of the dense tangles using three different reconnection criteria (geometrical G, geometrical-energetic GEm and dynamical D) and identified which properties are robust and which are sensitive to the choice of the criterion. We found the following: (1) the reconnection rate is a property directly related to the choice of the criterion. We concluded that the reconnection rate is similar for GE and D criteria albeit their different physical interpretations. On the other hand, in simulations with GC, the reconnection rate is significantly higher. The detailed analysis shows that most of the reconnections according to GC lead to an increase of the total length and to the creation of a very large number of small loops and loop fragments. The small loops removal procedure is therefore an essential part of the algorithm for this criterion. (2) One of the main parameters, $\mathcal{L}$, depends on the choice of the reconnection criterion for high temperature and strong counterflow velocities, when the tangle become dense. GC lead to sparser tangle, while DC gives the most dense tangle for the same T and $V_{\rm ns}$. As a consequence, the coefficient γ differs beyond measurement errors. Our results for γ agree well with available data. Thus the sensitivity of $\mathcal{L}$ to the choice of the reconnection criterion may explain the spread of the results for γ as found in literature. (3) In agreement with previous studies, we found that the vortex tangle is oblate and isotropic in the direction perpendicular to the counterflow. We observed a slight $V_{\rm ns}$ dependence of $I_{||}$ for $T = 1.6$ and 1.9 K for G and GE criteria. For all temperatures, the tangle was most oblate for GC and least oblate for DC. (4) The tangle drift velocity and the mutual friction force density depend on the choice of the reconnection criterion at moderate and high temperatures, with the corresponding coefficients being largest for DC and smallest for GC. This is similar to the behavior of the vortex line density. (5) The local tangle structure—the mean and RMS curvature of the tangle as well as PDFs of the loops length and curvatures—are only slightly dependent on the reconnection criterion. (6) The autocorrelation of the vortex orientation is practically independent of the choice of the reconnection criterion. Despite some clear differences in some results obtained with different reconnection criteria, the vortex filament method may be considered robust and well-suited for the description of the steady-state vortex tangle in the counterflow provided the results are interpreted having in mind the found values of the spread due to particular details of implementation.

We believe that the numerical results obtained in this paper at low, medium, and high temperatures T (1.3, 1.6, and 1.9 K) and their analysis will help in further studies of counterflow turbulence. In a very interesting zero-temperature regime (below 0.5–0.8 K), one should account for a set of additional effects caused by Kelvin waves: the energy cascade toward small scales [70–83], the damping of Kelvin waves, excited by reconnections due to mutual friction [84], and the slowdown of vortex rings, caused by thermally exited Kelvin waves [35]. The description of the Kelvin-wave effects requires either much higher spatial resolution within the vortex-filament method or the Gross-Pitaevskii approach. This is beyond the scope of this paper.

ACKNOWLEDGMENTS

This paper had been supported in part by the Minerva Foundation, Munich, Germany and by Grant 13-08-00673 from RFBR (Russian Foundation of Fundamental Research). L.K. acknowledges the kind hospitality at the Weizmann Institute of Science during the main part of the project. We are grateful to W. F. Vinen and L. Skrbek for their important comments, criticism and suggestions. We also thank S. K. Nemirovskii, N. J. Zabusky, and P. Mishra for their comments on the manuscript.

[1] M. Blažková, D. Schmoranzer, and L. Skrbek, Phys. Rev. E **75**, 025302(R) (2007).
[2] D. Charalambous, L. Skrbek, P. C. Hendry, P. V. E. McClintock, and W. F. Vinen, Phys. Rev. E **74**, 036307 (2006).
[3] J. Jäger, B. Schuderer, and W. Schoepe, Phys. Rev. Lett. **74**, 566 (1995).
[4] S. R. Stalp, L. Skrbek, and R. J. Donnelly, Phys. Rev. Lett. **82**, 4831 (1999).
[5] S. Fuzier, B. Baudouy, and S. W. Van Sciver, Cryogenics **41**, 453 (2001).
[6] Y. Nago, T. Ogawa, A. Mori, Y. Miura, K. Obara, H. Yano, O. Ishikawa, and T. Hata, J. Low. Temp. Phys. **158**, 443 (2010).
[7] J. Maurer and P. Tabeling, Europhys. Lett. **43**, 29 (1998).
[8] P.-E. Roche, P. Diribarne, T. Didelot, O. Français, L. Rousseau, and H. Willaime, Europhys. Lett. **77**, 66002 (2007).
[9] W. F. Vinen, Proc. R. Soc. Lond. A **240**, 114 (1957); **240**, 128 (1957); **242**, 493 (1957).
[10] W. F. Vinen, Proc. R. Soc. Lond. A **243**, 400 (1958).
[11] R. T. Wang, C. E. Swanson, and R. J. Donnelly, Phys. Rev. B **36**, 5240 (1987).
[12] R. K. Childers and J. T. Tough, Phys. Rev. B. **13**, 1040 (1976).
[13] J. T. Tough, Prog. Low Temp. Phys. **8**, 133 (1982).
[14] T. Zhang and S. Van Sciver, Nat. Phys. **1**, 36 (2005).
[15] T. Zhang and S. Van Sciver, J. Low Temp. Phys. **138**, 865 (2005).
[16] C. F. Barenghi, A. V. Gordeev, and L. Skrbek, Phys. Rev. E **74**, 026309 (2006).
[17] S. Babuin, M. Stammeier, E. Varga, M. Rotter, and L. Skrbek, Phys. Rev. B **86**, 134515 (2012).
[18] K. W. Schwarz, Phys. Rev. B **31**, 5782 (1985).
[19] K. W. Schwarz, Phys. Rev. B **38**, 2398 (1988).

[20] A. T. M. de Waele and R. G. K. M. Aarts, Phys. Rev. Lett. **72**, 482 (1994).
[21] R. G. K. M. Aarts and A. T. A. M. de Waele, Phys. Rev. B **50**, 10069 (1994).
[22] H. Adachi, S. Fujiyama, and M. Tsubota, Phys. Rev. B **81**, 104511 (2010).
[23] R. A. Ashton, L. B. Opatowsky, and J. T. Tough, Phys. Rev. Lett. **46**, 658 (1981).
[24] C. J. Gorter and J. H. Mellink, Physica **15**, 285 (1949).
[25] L. Skrbek and K. R. Sreenivasan, Phys. Fluids **24**, 011301 (2012).
[26] Makoto Tsubota, Michikazu Kobayashi, and Hiromitsu Takeuchi, Phys. Rep. **522**, 191 (2013).
[27] Sergey K. Nemirovskii, Phys. Rep. **524**, 85 (2013).
[28] C. F. Barenghi, V. L'vov, and P.-E. Roche, arXiv:1306.6248.
[29] David C. Samuels, Phys. Rev. B **46**, 11714 (1992).
[30] J. Koplik and H. Levine, Phys. Rev. Lett. **71**, 1375 (1993).
[31] R. Tebbs, A. J. Youd, and C. F. Barenghi, J. Low Temp. Phys. **162**, 314 (2010).
[32] M. Leadbeater, T. Winiecki, D. C. Samuels, C. F. Barenghi, and C. S. Adams, Phys. Rev. Lett. **86**, 1410 (2001).
[33] S. Nazarenko and R. West, J. Low Temp. Phys. **132**, 1 (2003).
[34] S. Ogawa, M. Tsubota, and Y. Hattori, J. Phys. Soc. Jpn. **71**, 813 (2002).
[35] G. Kristovic and M. Brachet, Phys. Rev. B **83**, 132506 (2011).
[36] N. G. Berloff and A. J. Youd, Phys. Rev. Lett. **99**, 145301 (2007).
[37] C. Nore, M. Abid, and M. E. Brachet, Phys. Rev. Lett. **78**, 3896 (1997).
[38] M. Kobayashi and M. Tsubota, Phys. Rev. Lett. **94**, 065302 (2005).
[39] M. Abid, C. Huepe, S. Metens, C. Nore, C. T. Pham, L. S. Tuckerman, and M. E. Brachet, Fluid Dyn. Res. **33**, 509 (2003).
[40] R. Numasato, M. Tsubota, and V. S. L'vov, Phys. Rev. A **81**, 063630 (2010).
[41] N. Sasa, T. Kano, M. Machida, V. S. L'vov, O. Rudenko, and M. Tsubota, Phys. Rev. B **84**, 054525 (2011).
[42] A. W. Baggaley, J. Laurie, and C. F. Barenghi, Phys. Rev. Lett. **109**, 205304 (2012).
[43] A. W. Baggaley, L. K. Sherwin, C. F. Barenghi, and Y. A. Sergeev, Phys. Rev. B **86**, 104501 (2012).
[44] M. Tsubota and M. Kobayashi, in *Progress of Low Temperature Physics*, Vol. 16, edited by M. Tsubota and W. P. Halperin (Elsevier, Amsterdam, 2009), p. 1.
[45] M. S. Paoletti, M. E. Fisher, and D.P. Lathrop, Physica D **239**, 1367 (2010).
[46] D. Kivotides, J. Fluid Mech. **668**, 58 (2011).
[47] D. C. Samuels and D. Kivotides, Phys. Rev. Lett. **83**, 5306 (1999).
[48] Makoto Tsubota, Tsunehiko Araki, and Sergey K. Nemirovskii, Phys. Rev. B **62**, 11751 (2000).
[49] Luiza P. Kondaurova and Sergey K. Nemirovskii, J. Low temp. Phys. **138**, 555 (2005).
[50] Luiza P. Kondaurova, Vladimir A. Andryuschenko, and Sergey K. Nemirovskii, J. Low Temp. Phys. **150**, 415 (2008).
[51] Luiza P. Kondaurova, Vladimir A. Andryuschenko, and Sergey K. Nemirovskii, Computational Technologies **15**, 41 (2010) (in Russian).
[52] A. Baggaley, J. Low Temp. Phys. **168**, 18 (2012).
[53] C. F. Barenghi, D. C. Samuels, JLTP **156**, 281 (2004).
[54] Sergey K. Nemirovskii, Phys. Rev. Lett. **96**, 015301 (2006).
[55] D. R. Poole, H. Scoffield, C. F. Barenghi, and D. C. Samuels, J. Low Temp. Phys. **132**, 97 (2003).
[56] Ronald Aarts, Ph.D. thesis Technische Universiteit Eindhoven, 1994.
[57] F. R. Hama, Phys. Fluids **6**, 526 (1963); R. J. Arms and F. B. Hama, *ibid*. **8**, 553 (1965).
[58] K. W. Schwarz, Phys. Rev. Lett. **49**, 283 (1982).
[59] G. W. Rayfield and F. Reif, Phys. Rev. **136**, A1194 (1964).
[60] R. J. Donnelly and C. F. Barenghi, J. Phys. Chem. Ref. Data **27**, 1217 (1998).
[61] W. H. Press, B. P. Flannery, S. A. Teukolsky, and W. T. Vetterling, *Numerical Recipies, The Art of Scientific Computing* (Cambridge University Press, New York, USA, 1986).
[62] K. P. Martin and J. T. Tough, Phys. Rev. B **27**, 2788 (1983).
[63] Y. Mineda, M. Tsubota, and W. F. Vinen, J. Low Temp. Phys. **171**, 511 (2013).
[64] C. Bauerle *et al*., Nature (London) **382**, 332 (1996); C. B. Winkelmann, J. Elbs, Yu. M. Bunkov, E. Collin, H. Godfrin, and M. Krusius, Nucl. Instrum. Meth. A **574**, 264 (2007).
[65] D. D. Awschalom, F. P. Milliken, and K. W. Schwarz, Phys. Rev. Lett. **53**, 1372 (1984).
[66] V. Arp, Cryogenics **10**, 96 (1970).
[67] H. C. Kramers, T. M. Wiarda, and A. Broese van Groenou, *Proc. LT7* (University of Toronto Press, Ontario, Canada, 1961), p. 562; H. C. Kramers, in *Superfluid Helium*, edited by J. F. Allen (Academic, London, 1965), p. 199.
[68] C. E. Swanson and R. J. Donnelly, J. Low Temp. Phys. **61**, 363 (1985).
[69] S. K. Nemirovskii, Phys. Rev. B **57**, 5972 (1998).
[70] E. Kozik and B. Svistunov, Phys. Rev. Lett. **92**, 035301 (2004).
[71] J. Laurie, V. S. L'vov, S. Nazarenko, and O. Rudenko, Phys. Rev. B **81**, 104526 (2010).
[72] V. S. L'vov and S. Nazarenko, JETP Letters **91**, 428 (2010).
[73] E. Kozik and B. Svistunov, Phys. Rev. B **82**, 140510(R) (2010).
[74] V. V. Lebedev and V. S. L'vov, J. Low Temp. Phys. **161**, 548 (2010).
[75] V. Kozik and B. V. Svistunov, J. Low Temp. Phys. **161**, 603 (2010).
[76] V. V. Lebedev, V. S. L'vov, and S. V. Nazarenko, J. Low Temp. Phys. **161**, 606 (2010).
[77] L. Boue, R. Dasgupta, J. Laurie, V. S. Lvov, S. Nazarenko, and I. Procaccia, Phys. Rev. B **84**, 064516 (2011).
[78] L. Boue, V. S. L'vov, and I. Procaccia, Europhys. Lett. **99**, 46003 (2012).
[79] E. B. Sonin, Phys. Rev. B **85**, 104516 (2012).
[80] V. S. L'vov, and S. V. Nazarenko, Phys. Rev. B **86**, 226501 (2012).
[81] G. Krstulovic, Phys. Rev. E **86**, 055301(R) (2012).
[82] A. W. Baggaley and J. Laurie, arXiv:1204.4034v3.
[83] D. Proment and C. F. Barenghi, arXiv:1308.0852.
[84] R. Hänninen, Phys. Rev. B **88**, 054511 (2013).